POLITECNICO DI TORINO

Master's Degree in ICT for Smart Societies

Master's Degree Thesis

A Machine Learning Approach in Pendant Drop Tensiometry Using Image Moments

Supervisors

Prof. Enrico MAGLI

Prof. Thomas BECKER

Candidate

Can AKGOL

2022

Abstract

One of the most recent emerging technique for Surface Tension caluclation is called Pendant Drop Tensiometry which is a Axisymmetric Drop Shape Analysis. Machine Learning and Neural Networks are another fields which are emerging and could be commonly used for any kind of topic. Although Pendant Drop Tensiometry and Machine Learning are inevitably improving fields separately, there are not many works previously in which both fields are merged to solve a problem. We have followed to main works and first main work [1] helped this thesis to extract and understand the usage of differential equations of Pendant Drop Tensiometry. Other recent work [2] could be interpreted as the only recent work which could be useful to create the hypothesis of this master thesis since it combined a Machine Learning approach with Pendant Drop Tensiometry. This Machine Learning approach consist of a Neural Network approach to predict indirectly Surface Tension via measuring non-dimensional gravitational control parameter and non-dimensional apex pressure. These two non-dimensional parameters are the key parameters and predicted parameters by the Neural Network which leads to the computation of Surface Tension. This was an indirect approach that is also the approach in this thesis too. Before applying a Machine Learning approach to Pendant Drop Tensiometry, Young-Laplace equation was written in terms of differential equations and then, they are solved iteratively together with image analysis techniques using digital images captured from a camera.

This thesis builds a bridge between Pendant Drop Tensiometry and Machine Learning once but the aim is to present an innovative and much simpler solution since the previous Machine Learning approach was quite complex and computationally demanding. The main objective of this thesis is to provide a Machine Learning approach in Pendant Drop Tensiometry using Image Moments in order to predict Surface Tension of pendant drops. This Machine Learning approach based on a Neural Network architecture to predict non-dimensional parameters according to regions which are defined according to validity of non-dimensional parameters. This validity of non-dimensional parameters are considered according to shape factor of a pendant drop since very most likely pendant drop shapes have a shape factor equal to 2 or 3. These valid regions are defined with calculated curves in a graph. After extracting non-dimensional parameter values from valid regions, these values are used to create synthetic pendant drop shapes. Image Moments takes the role after this point and image moments of synthetically generated drop images are calculated to feed Neural Network architecture. Image Moments are the innovation because they are scale, translation and rotation invariant to create a robust networks to make the algorithm work for also rotated, scaled and translated pendant drop image versions. Non-dimensional parameters are calculated individually in separate Neural Networks and corresponding Mean Square errors were approximately 0.021. Previous Machine Learning approach [2] was trained for 3 weeks but this thesis only took hours for measuring Surface Tension which is the proof that, the aim, which is to create simpler model using Image Moments, was achieved consequently.

Keywords: Pendant Drop Tensiometry, Surface Tension, Machine Learning, Neural Networks, Image Moments, Non-Dimensional Apex Pressure, Non-Dimensional Gravitational Parameter, Synthetic Dataset

Summary

Several techniques were proposed by scientists to calculate interfacial tension of a liquid. Most of the techniques require a physical human effort also after installing the setup to measure the interfacial tension and related metrics and variables dependent to interfacial tension. Pendant Drop Tensiometry is an experimental method to further improve these techniques in terms of measuring interfacial tension and related metrics. This thesis work is dedicated to measure Surface Tension of Pendant Drops with using Machine Learning techniques by observing different types of Pendant Drop forms. This is called Axisymmetric Drop Shape Analysis. Various forms of Pendant Drops are constructed synthetically, and Machine Learning Model is applied first to Synthetic Images in order to predict some metrics which is needed for calculating the Surface Tension of a Pendant Drop. Then, algorithm is verified by using real data instead of just testing synthetic image data. Image Moments of the created Pendant Drop images are used as the key features to predict Surface Tension. There is no need of physical instruments or a complicated setup for that calculation. Everything that is needed to apply an automatized algorithms to a captured image of a drop. The improvement in GPU providers dramatically increased the use of Machine Learning Models for image analysis and big data analysis. This thesis work is used to present how the improvements in Machine Learning are combined with the improvements in Pendant Drop Tensiometry to calculate the Surface Tension and related metrics.

Acknowledgements

This thesis work represents an emotional end and a journey which is full of effort. This journey started in Politecnico di Torino and ends in Technical University of Munich. First of all, having completed university in Turkey and follow a master program in Politecnico di Torino and writing Master Thesis in Technical University of Munich is the proof of that, I am always willing to take on challenges no matter how big or small. Secondly, I must thank to every single person who has believed me with no doubt. I always welcomed friendly both in PoliTo and TUM as a foreign student by other students and professors. After completing a course with Prof. Enrico Magli in the first semester of my Master program, I was dedicated to write my thesis with the professor. Additionally, my supervisor and the team in TUM always made me feel at home too even if it was a shorter journey than I had in PoliTo. Especially, I need to thank to Ivan Pribec, Dr. Ehsan Fattahi and Prof. Thomas Becker who always supported during my exchange stay in TUM. I would like to thank my best friends: Paolo and Francesco who always helped me and accompanied me while reaching to final work of this master program. My dear friend Onur from San Diego always supported me and he deserves most of my thanks because he has been stayed by my side since the beginning of my bachelor's degree years. Most important person for me was Merve who has never stopped trusting me and stayed with me as my other half. She is the person who I will share rest of my life. Finally, the biggest thanks are for my family. My father Atilla, my mother Nuray, my aunt Gulay, my uncle Kaan and my cousin Nazli. I owe them every success I have achieved, and I will never forget their every kind of support.

Table of Contents

List of Tables

List of Figures

Acronyms

AI
: Artificial Intelligence

BGT
: Brau- und Getränketechnologie

TUM
: Technical University of Munich

PCA
: Principal Component Analysis

FNN
: Feedforward Neural Networks

CNN
: Convolutional Neural Networks

RNN
: Recurrent Neural Networks

ReLU
: Rectified Liner Unit

ADSA
: Axisymmetric Drop Shape Analysis

CCD
: Charged Coupled Device

CSF

Conventional Shape Fitting

ODE

Ordinary Differential Equations

MSE

Mean Square Error

MARE

Mean Absolute Relative Error

Chapter 1

Introduction

This master thesis work is intended to implement a automatized system to determine the surface tension of a pendant drop, which is about to detach under the capillary tube of a needle, using Machine Learning algorithm and Image Moments. Main objective of this thesis work is to predict non-dimensional apex pressure and non-dimensional gravitational control parameter of a pendant drop from a synthetic image by using Neural Network and Image Moments which is directly computed from synthetically generated images of different variants of Pendant Drops. Most challenging part is to predict these non-dimensional parameters with high precision because non-dimensional parameter values are very close numerical values which requires a precise prediction success. This thesis is planned to provide an innovative implementation to predict surface tension of a pendant drop in a more simple way than it has done before in several experiments. Innovative part of the thesis is using Image Moments of a pendant drop image and the simpler part is creating a simpler Neural Network architecture when it is compared to previous works. Main previous work that is considered in this thesis work is a scientific paper which was published on June 2020 by Felix S. Kratz [2] who is also provided the only work using Neural Networks to predict surface tension.

Main motivation on this thesis topic is that, I was always thrilled by physics and Machine Learning applications so this thesis provided the perfect opportunity by using an innovative idea such as Image Moments which made me more thrilled due to feeling like I am somehow inventing something new using my ambitions.

This chapter is formed by 3 different parts: Interfacial Tension(Surface Tension), Problem Description and Chapter Explanations. First part is to introduce the theory behind the Surface Tension algorithms to have a better insight during reading the rest of this master thesis. Problem description stands for the answer to questions: “Why is this thesis work done?”, “What is the hypothesis of this master thesis and how is the hypothesis investigated?”. Chapter Explanation part explains how this thesis is organized.

1.1 Interfacial Tension(Surface Tension)

Term Surface Tension is the main target in this project because all of the algorithm is designed to obtain the surface tension of a bubble liquid which is hanging from a capillary tube. Surface Tension should be observed under the title of Interfacial Tension because it is a more specific term. Interfacial Tension is the scientific term that is a relational property between any two substances. This relation could be liquid-liquid, liquid-gas, liquid-solid and solid-gas. On the other hand, surface tension is the specific relational property between liquid and gas [3]. Interfacial tension or surface tension is represented by the gamma symbol and the SI unit of interfacial tension is millinewton per meter(mN/m) which is a representation of force per unit length. It is also defined as a measure of how much energy is required to make a unit area of interface between two immiscible liquids which corresponds to units of Joules per square meter [1].

Figure 1.2 illustrates that, Interfacial Tension is the key point to keep two substances independent and prevent spreading of a liquid over a solid.

Figure 1.1: Cohesion and Adhesion Forces Applied to Water Drops on a Leaf

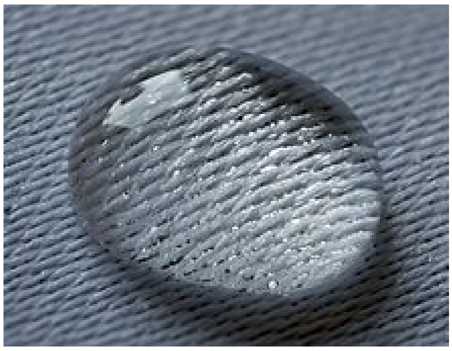

Figure 1.2: Surface Tension that Keeps a Water Droplet Tight [4]

In order to have a better understanding of these two tension terms, adhesion and cohesion terms should be presented too. Adhesion stands for the interaction between two different molecules which are immiscible, but Cohesion stands for the attraction between the molecules which are likely [3]. It creates cohesive forces between likely molecules, so these molecules stay connected or 'resists' to separate from each other. Water has strong cohesive forces and cohesion is the dominant property in Figures 1.2 and 1.1, but still adhesive forces exist. Figure 1.3 also a great example to realize the cohesive force between water molecules. The cohesive force diagram in Figure 1.3 shows how the water molecules are attached and 'resists' towards detachment[3].

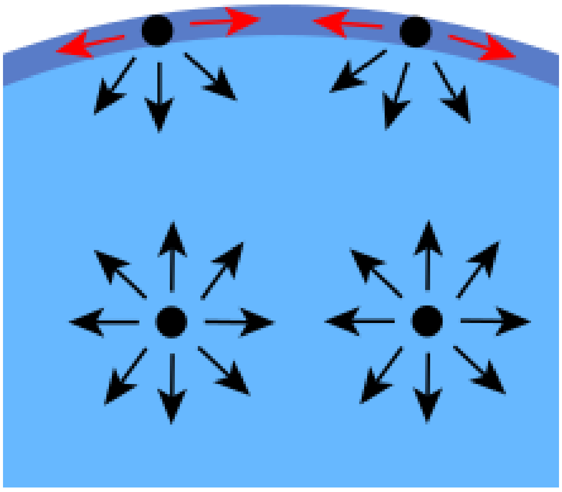

Figure 1.3: Cohesive Forces in a Liquid [4]

When you relate these concepts to this thesis work cohesive forces becomes dominant again. Cohesive forces create a tight molecular connection between molecules before the detachment of a bubble from a capillary tube. Before this detachment, Pendant Drop Tensiometry method is applied when the drop reaches to its highest volume which is only possible with cohesive forces between molecules for that specific used liquid in the experiment. Surface Tension could also be defined as the property of fluids related to cohesive forces that is responsible for: shape of droplets, formation of bubbles and thin films, and wetting of surfaces (hydrophobic, hydrophilic).

Additionally, surface tension has an industrial importance too. It is a widely deep measure for chemistry and physics related companies and products of companies. There are many examples such as food and beverage production, paints and polymer coatings, inks and printing, emulsions, flooding, quality testing of hydrophobic liquids, injection molding and finally commercial products like shampoo etc. As it can be seen from the various number of examples, this surface tension measuring is a very popular and a trending problem for the significant part of the industry. For instance, interfacial tension is beneficial in terms of observing emulsifiability and the tendency for the phases to separate [5]. It is also a critical measure in medicine for doctors to investigate surface tension of blood serum, spinal fluid and gastro juice[John Moore Andreas] but in this theses the solutions is more concentrated for the purposes of Brau- und Getränketechnologie (BGT) Department in Technical University of Munich (TUM) which are not mainly based on medicine. As a consequence, Surface Tension is measured using pendant drop tensiometry technique as a final step in this thesis work.

1.1.1 Pendant Drop Tensiometry

Tensiometry is a scientific method to obtain the interfacial or surface tension which is first proposed more than a century ago by Worthington [6] and tables are prepared by Bashfort [7] which contains approximate solutions to the axisymmetric Young-Laplace equation. Bashfort tried to extract precise and accurate tables which could be helpful for extracting the interfacial tension parameter from a shape analysis of a pendant drop. This Young-Laplace equations now located in the hearth of this pendant drop method. More detailed explanation and theoretical background could be found in the section Background and Preparation to New Methodology about the Young-Laplace equation.

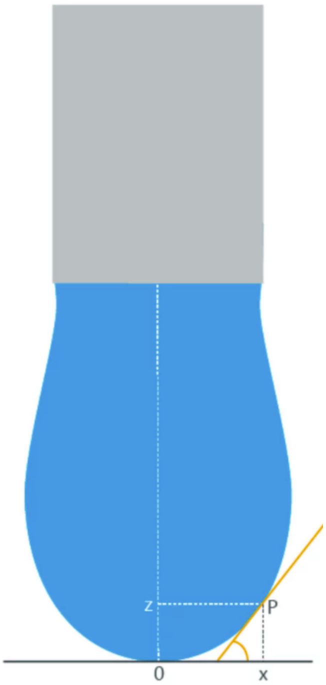

Figure 1.4: Artificial Example of a Pendant Drop Profile [8]

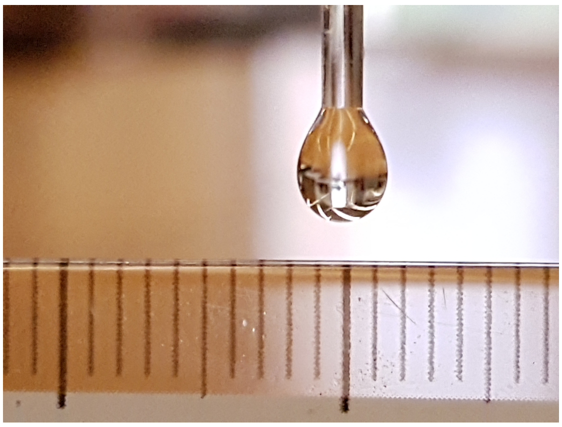

Figure 1.5: Experimental Pendant Drop Example in Real Scenario

The procedure followed in pendant drop, to calculate boundary tension of a liquid, is a fast method which leads to high precision. Before the application of Machine Learning to Pendant Drop method, images are analyzed directly without using any Machine Learning algorithms. In Figure 1.4 an artificial example of a pendant drop is shown which is an instant just before the detachment of a liquid from a capillary tube. Meanwhile, a real example of a pendant drop is shown in Figure. The capillary tube and the drop can be obviously seen from the Figure 1.5 too. During image capturing process in pendant drop method image is captured together with capillary but one problem about this technique is that capillary should be further removed because image analysis to determine interfacial tension of a drop must be applied only on the drop shape. Finally the Young-Laplace Equation is applied iteratively for the image analysis of the captured axisymmetric pendant drop image. Fitting the Young-Laplace equation is a complicated and demanding computational process.

Figure 1.6: Experimental Setup of Pendant Drop Tensiometry Application [9]

Figure 1.6 illustrates the experimental setup that is needed for pendant drop tensiometry method. It is actually a simple setup which includes a camera, a light source and a needle to form the pendant drop. The problems that can occur will be explained in Chapter 3.

Furthermore, as it is explained in the beginning of this chapter one of the most critical part which is needed to understand well is adhesive and cohesive forces part. Cohesive forces subject to strong mutual attractions which leads to uniformly balanced drop in each direction and creates an internal pressure. These attractions could be kind of a synonym of contraction on the surface of a liquid in which the internal end external contractions create the surface tension of a pendant drop[JohnMooreAndreas]. The reason behind drop remains attached with the capillary tube is that the adhesive forces are bigger than the gravitational force. Consequently, adhesive and cohesive forces are important due to playing an active role for determining the surface tension using pendant drop method.

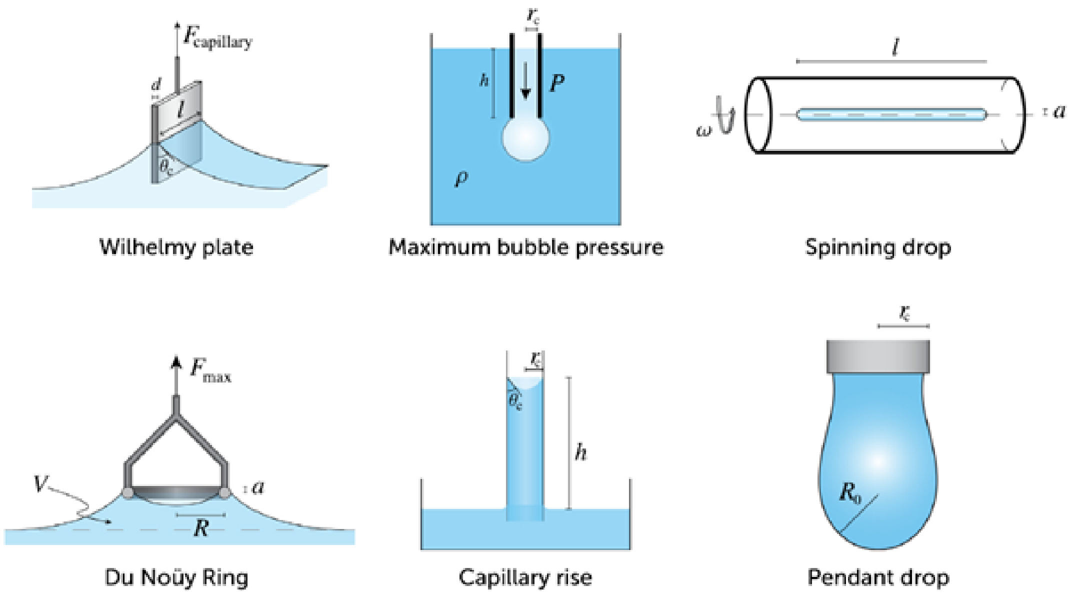

Figure 1.7: Different Techniques to Measure Interfacial Tension. Reprinted from [1], with the permission of Elsevier Publishing.

Many methods are proposed to measure surface tension as you can see from Figure 1.7. Pendant drop method is agreed as the most rapid and robust technique to obtain the interfacial tension. All these methods has an old history and some of them are old-fashioned solutions. This Figure is taken by the scientific paper by Berry [1] and all methods to determine interfacial tension are explained quickly regarding to Figure 1.7 as following:

- **Wilhelmy Plate:** In this method, a vertical thin plate is placed between a liquid-liquid interface. This wettable plate is lifted with a force and the interfacial tension is calculated directly using that force and the perimeter of the plate [10].

- **Maximum Bubble Pressure:** A thin-edged tube is placed to a liquid in order to create the maximum pressure with the help of edges. This pressure causes the formation of a gas bubble inside the liquid at the bottom of the thin-edged tube. Surface tension is a measure which could be considered as that pressure that us created by the thin-edged tube.

- **Spinning Drop:** Two liquids are injected to a vertical cylinder. One liquid is the drop which is in the middle of the vertical cylinder and the other liquid is the surrounding liquid. This method is based on the gravitational acceleration and the density difference between drop liquid and the surrounding liquid. Using density difference between liquids and using gravitational acceleration, which is the result of the spinning move of the vertical cylinder, interfacial tension is measured directly [5].

- **Du Nouy Ring:** This method is also a microbalance measurement method for measuring interfacial tension at fluid-fluid interfaces [10] and the method is based on a force acting on a wettable ring. Horizontal ring is moved upwards direction to a certain height as it is done in the Wilhelmy plate method and the interfacial tension is calculated using force applied and the perimeter of the horizontal ring [10].

- **Capillary Rise:** The main objective in this method is to create three interfaces by placing a vertical tube into a liquid. This liquid could be also formed by two different liquids or a liquid and a gas form substance. The capillary placed inside the liquid provides the equilibrium state between three boundary tensions. For this method, specific value of an angle of contact with the wall and balanced pressure at any point in the liquid surface is needed for equilibrium state[andreas]. This method is just applicable to pure and non-viscous liquids which is a limitation of this method too[andreas].

All these methods are explained very detailed in the Drelich's work [10] and not explained detailed in this thesis because main concentration in this thesis is pendant drop method due to being more efficient and a modern technique. Some commercial solutions also exist, which presumably all rely upon classic shape analysis, but pendant drop tensiometry is an axisymmetric drop shape analysis technique that is needed by TUM because BGT Department in TUM has the pendant drop device. This device is used originally for bottle cleaning duty. In a beverage bottling plant, bottles are washed. During this washing procedure if some soap remains in the bottle, it can be detected by the pendant drop device. The second reason BGT has it, is to study some beer Ingredients which affect foam stability.

1.2 Problem Description

The main objective of this thesis work is to build a machine learning approach for pendant drop tensiometry method using image moments in order to be able to predict surface tension γ. Although this is the major objective of this project, there are minor objectives to create an innovative and simpler solution to this problem too. Previous works are not simple and computationally demanding. Other solution methods to this problem are explained in the previous section in order to explain how this thesis work overcome these previous methods. The main scientific paper that is followed in this thesis is the paper by Kratz [2] which is published in June 2020. It is a very current work so the problem for determining surface tension of a pendant drop is an emerging issue. Kratz is the only and last person used Machine Learning integrated with Axisymmetrical Drop Shape Analysis, so it is also aimed to prepare an alternative, progressive and innovative machine learning model to fill the gap in this area. For all previous works, it is aimed to have a rapid solution and the current technological world is always demanding more rapid solution. That's why this thesis work is done. Goal was to develop a new drop shape analysis algorithm using Machine Learning and image moments and the hypothesis was: Image Moments are helpful and enough to predict Surface Tension using Deep Learning. Image moments are never used for predicting surface tension. Image moments are another key to reach success. Deep learning is decided to be used as the machine learning approach and dataset is formed synthetically using synthetic drop shapes.

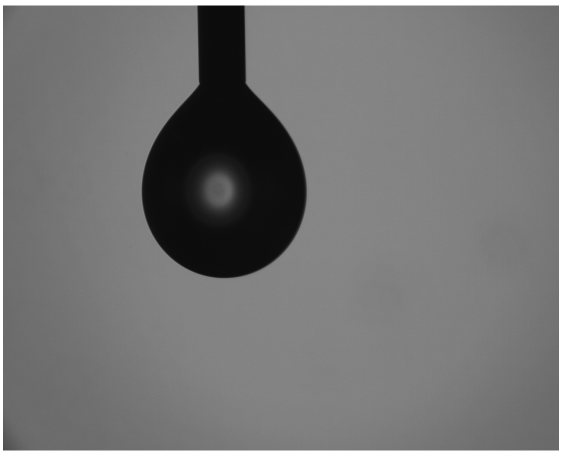

Figure 1.8: Real Scenario Image taken from the Berry's Experiment [11]

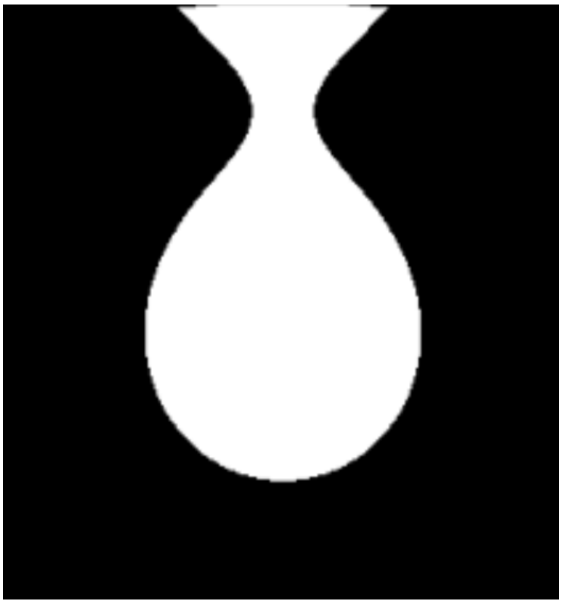

Figure 1.9: Synthetically Generated Gray-scale Pendant Drop Example

In Figure 1.9 a real scenario image is presented and the Figure 1.8 represents one example of drop shape that is created synthetically serving Image Moment calculation purpose to prepare dataset. Problem in this point is to validate the model using synthetic dataset. In other words, the training is done just using synthetic images but the testing phase includes parameters from both real scenario and synthetic images. If the validation on real scenario images reaches to success, it can be reported as using image moments and synthetic dataset is the completely correct methodology to determine surface tension. Followed steps to prepare a synthetic dataset and a Deep Learning algorithm are detailed described in Section 3.

1.3 Chapter Explanations

This thesis is organized as the following:

- **Background of Theory and Preparation to New Methodology:** This part explains all the details behind the theory of pendant drop tensiometry and related machine learning background which could be useful to have a better connection what is done for the actual implementation. In this section, it is also explained that which sources and methods affected this thesis work and what kind of a path was followed through it. It has been discussed how the similar methods that were used before, and it is discussed that what kind of problems this thesis is inspired by.

- **Proposed Methodology:** Here are the connections between the approaches in Machine Learning and approaches in Pendant Drop Tensiometry are explained as a project in which the way of connections has never addressed before in any other project. The reason behind the usage of this method is explained and the implementation steps are described step by step. methods affected this thesis work and what kind of a path was followed through it. It has been discussed how the similar methods that were used before were improved by the methodology provided by this thesis and how methods were adjusted in order to make methods usable for our purpose.

- **Experimental Results and Discussion:** In this chapter, results of the machine learning algorithm are discussed, and inferences are discussed in terms of the success of the methodology. Performance of the methodology is observed with different statistical parameters that can be used for determining success of the thesis work. Hypothesis is tested and supported by results.

- **Conclusion and Future Works:** This chapter is to sum up the whole project and give the main idea to the reader one more time by supporting with obtained result in a very short way. Additionally, this chapter is a critical part which stores hints to move on with new methodologies over this thesis work. It is described that this thesis could still have parts to be improved and several ways are proposed for this purpose to help people who are working on this area.

Chapter 2

Background of Theory and Preparation to Methodology

This chapter begins with Machine Learning basics and various themes related with Machine Learning. Machine Learning concept is presented detailed because it should be understood well why it is used in this technique and what other kinds of Machine Learning algorithms could be considered to apply. After this deep introduction to Machine Learning themes, problems, physics behind the theory of pendant drop will be explained to show how it is adjusted and prepared to the new methodology that is provided in this thesis work. Image Moments and their applications will be presented to give a hint about the proposed methodology. Finally, all the critical concepts and parameters used in proposed methodology are explained and a brief description of previous pendant drop tensiometry method without a machine learning approach will be presented to be able to make a better comparison between this innovative thesis work. Chapter begins with Machine Learning and Deep Learning concepts to express what is the theory background thesis' algorithm.

2.1 Machine Learning

Artificial Intelligence (AI) is a trending and rapidly developing popular theme in the world. AI makes possible for computers to imitate human decisions. Therefore, Machine Learning could be classified as the subtopic of AI. Machine Learning is more statistical and probabilistic based method set. Machine Learning makes possible the detection of patterns in data in an automatized way. Then, the detected pattern is used to predict the future possible pattern or used to make inference about the new data. Data is always the key for the Machine Learning methods, so the probability and statistics are the underlying mathematical methodology. Training set and test set are named for these purposes. During the training process pattern is recognized and it is tested on the test set to verify that the algorithm could detect the pattern successfully or not. As the data is the key for the success, Machine Learning problems are split into two: *Supervised Learning* and *Unsupervised Learning*.

2.1.1 Supervised Learning

Supervised Learning has a goal of learning the pattern from an input data x to mapping it to an output data y where x and y are the pairs of a training set. Input data x can be named as features and the output data y can be named as labels. Features that belong to a particular labeled data has an unknown relation such as y = f(x) and an estimate f is determined to find an estimate y with the help of a Machine Learning algorithm. Supervised Learning is helpful to solve three different types of problems:

- **binary classification** can be 'Yes' or 'No' question, label y could be '0' or '1', so there are 2 possible classes.
- **multi-class classification** can result in more than 2 class predictions such as predicting different type of animals from images, so label y could be any class according to the defined label types in the dataset.
- **regression** can be an estimation of label y where y is a Real number.

In this thesis, regression based supervised learning is used as a Machine Learning approach. Since some numerical values are predicted instead of categorical classes as an output of the Neural Network.

2.1.2 Unsupervised Learning

Unsupervised Learning does not have a role to classify or categorize sample data according to its defined labels. There is only input data x but there is no existence of output y. Unsupervised learning investigates the similarities between sample data and reflects the similarities and similarity levels to the user according to used Machine learning technique. This is more similar to human learning. Unsupervised learning is helpful to solve some Machine Learning methods which are:

- **Clustering:** is a method to find groups of sample data such that sample data in that group will be similar. The sample data that are grouped should be consistent in terms of similarity with other data points in that particular group too. Patterns in groups should be similar, so the groups should be easily distinguishable among each other according to their similarities. Image segmentation could be a great example of clustering in which the images is broke up into meaningful similar regions. For instance, sky, sea and territory regions could be segmented with the help of clustering.

- **Principal Component Analysis (PCA)** is a technique which is used very often for people who are dealing with large dataset. The main goal in this technique is to apply dimensionality reduction to dataset without losing useful information about the whole dataset.

2.2 Deep Learning

Deep Learning is also have almost the same goal with Machine Learning methods which is to catch deterministic patterns to be able to predict the future data. Deep Learning could also be interpreted as a family member of Machine Learning. The main Deep Learning architecture is Neural Networks which is also includes the main work in this thesis. Neural Networks is a very useful tool and improved the state-of-the-art in various problems such as speech recognition, object pattern recognition and statistical machine translation. It is called "Deep" Learning due to having many layers in its architecture to learn representations of data. Deep Learning is a trending concept as the Figure 2.1 taken by Google Trends [12] illustrates the searches in Google since 2004. After 2014, the curve dramatically increased and Deep Learning papers hit the top level in the scientific paper topics.

Figure 2.1: Interest Over Time to Deep Learning Title on Google Searches [12]

Another factor that makes Neural Networks trending is the computing power. Deep Learning architectures requires high computing power. During the development of computing power, algorithms and models started to improve too. When all these developments are considered, it is inevitable to not use Deep Learning algorithms for experimental works. With the improvement in models and computing power, dealing with big data become easier and more realistic, so Deep Learning started to overcome standard Machine Learning algorithms like Nearest Neighbor, SVM, Decision Trees and Naïve Bayes. On the other hand, deeper networks still means that, it is computationally demanding due to increasing number of parameters in the deeper networks.

2.2.1 Neural Networks

Neural Networks has various forms for different purposes. *Feedforward Neural Networks* (FNN) can be used for regression or classification problems which cannot be solved linearly. There are no loops in this type of networks and they can become deep by adding many hidden layers. *Convolutional Neural Networks* (CNN) is a type of FNNs that share weights over layers. CNNs are used widely in visual learning and CNNs perform well for classifying images. For *Recurrent Neural Networks* (RNN), loops are allowed, so it is a dynamical system which makes it more difficult to train. RNNs are trained for speech recognition tasks.

Main Principles

In Figure 2.2, the basic element of Neural Network is introduced. It is called "*Perceptron*". It weights different inputs coming from input or previous layers to make a decision.

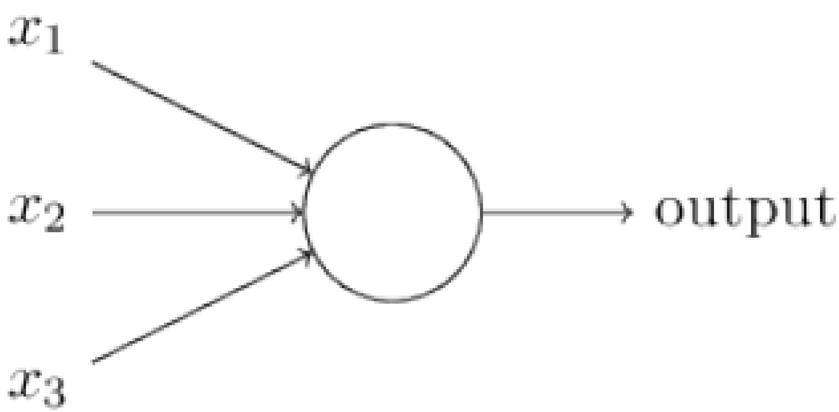

Figure 2.2: Perceptron

$$output = \begin{cases} 0, & \text{if } \sum_j w_j x_j \leq threshold. \\ 1, & \text{if } \sum_j w_j x_j > threshold. \end{cases} \tag{2.1}$$

In the Eq. 2.1, it explains how the decision is made in the most basic unit of Neural Networks where w_j is the weight for corresponding connection and x_j is the input parameter to a neuron.

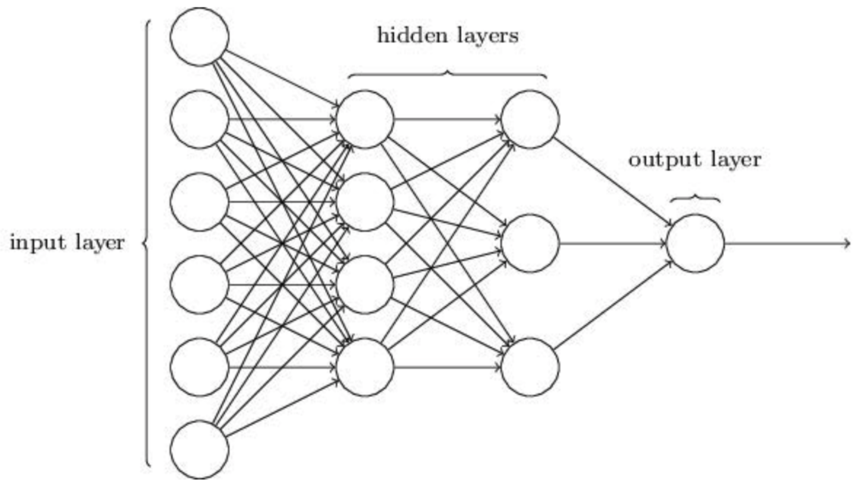

Figure 2.3: Basic Neural Network Architecture

Figure 2.3 shows a basic form of a complete Neural Network architecture. Each node is named as neuron, each set of vertical neurons named as layers. Where you feed the network with the features is called input layer and where you make the final decision is called output layer. The layers between input and output layers are called as hidden layers. Each node has its own activation function f(x) where x is the input as it is described in Figure 2.2 and nodes output could be input to another node which is in the next layer. Weighted sum of inputs affects the output decision as it is described in Eq. 2.1 This operation is iteratively done until reaching to the final decision at the output layer. Small change in the weights will result in a small change in the output layer too. The output layer could be formed by just one node or more than one node. If the problem is a binary classification problem or if a value tried to be regressed, the output layer will be formed by one neuron. If it is a multiclass classification, the output layer will be formed by more than one neuron. In this condition, the output is named as '*One Hot Vector*' because the node which provides the biggest probability in the output layer is chosen as the decision.

Activation Functions

Standard Machine Learning techniques generally have some limitations in terms of linear classifiers. Linear classifier provides a prediction based on linear combination of features x_j but Neural Networks is the key for switching to more flexible framework to eliminate the limitations of linear classifiers. *Activation Functions* are non-linear functions which are built inside nodes. There are many examples of activation functions but most common ones are explained in the Table 2.1.

ReLU	$f(x) = \begin{cases} 0 & \text{for } x \leq 0 \\ x & \text{for } x > 0 \end{cases}$
Softmax	$f_i(\vec{x}) = \frac{e^{x_i}}{\sum_{j=1}^{J} e^{x_j}} i = 1, ..., J$
Sigmoid	$f(x) = \frac{1}{1 + e^{-x})}$
tanh	$f(x) = \tanh(x) = \frac{(e^x - e^{-x})}{(e^x + e^{-x})}$

Table 2.1: Examples of Activation Functions

These activation functions are embedded to the smallest element of Neural Networks which is a node. Each node set in a layer has its own activation function. *Rectified Liner Unit* (ReLU) is the most common activation function because it has several advantages like being unbounded and monotonically increasing function. Even though ReLU works great with larger weights, the learning stops entirely with weights smaller than zero. To eliminate this problem, *LeakyReLU* activation function is introduced. Learning never stops with LeakyReLU even if it has smaller weights.

2.3 Image Moments

For image analysis task, *Image Moments* are a beneficial tool for extracting image features from a binary image. Image Moments are weighted average of pixel intensities that are extracted from an image [13], [14]. Image Moments are useful to extract a specific property of the image in which the user obtain a meaningful result [15].

The 2D continuous function in Eq. 2.2 is the definition of an Image Moments in which p and q are the orders of image moments.

$$M_{pq} = \iint_{-\infty}^{\infty} x^p y^q f(x, y) dx dy \tag{2.2}$$

Since it is the weighted average of pixel intensities, moments could also be adapted to scalar as it is done in Eqn. 2.3. I(x,y) are the pixel intensities adapted to a binary image. After this point, only the discrete equations will be presented due to working on digital images:

$$M_{ij} = \sum_x \sum_y x^i y^j I(x,y) \tag{2.3}$$

For simplicity, it can be interpreted as the sum of pixel intensities with considering the location of the pixels in the image. Location information sometimes removed from the equation. Since it can be applicable to binary images, another simple definition can be made: Sum of the number of white pixels in a grey-scale image or the area of the white region in a greyscale image. M_{00} is considered as the area of the object in a binary image and centroids are computed as in Eqn. 2.4.

$$\{\bar{x}, \bar{y}\} = \left\{ \frac{M_{10}}{M_{00}}, \frac{M_{01}}{M_{00}} \right\} \tag{2.4}$$

Centroids are used to calculate the central moments of the image which is shown in Eq. 2.5

$$\mu_{ij} = \sum_x \sum_y (x-\bar{x})^i (y-\bar{y})^j I(x,y) \tag{2.5}$$

Central moments are calculated up to the third central moment because Hu Moments will be calculated with using these central moments up to its third moment:

$$\begin{aligned}
\mu_{00} &= M_{00} \\
\mu_{01} &= 0 \\
\mu_{10} &= 0 \\
\mu_{11} &= M_{11} - \bar{x}M_{01} = M_{11} + \bar{y}M_{10} \\
\mu_{20} &= M_{20} - \bar{x}M_{10} \\
\mu_{02} &= M_{02} - \bar{y}M_{01} \\
\mu_{21} &= M_{21} - 2\bar{x}M_{11} - \bar{y}M_{20} + 2\bar{x}^2 M_{01} \\
\mu_{12} &= M_{12} - 2\bar{y}M_{11} - \bar{x}M_{02} + 2\bar{y}^2 M_{10} \\
\mu_{30} &= M_{30} - 3\bar{x}M_{10} + 2\bar{x}^2 M_{10} \\
\mu_{03} &= M_{03} - 3\bar{y}M_{01} + 2\bar{y}^2 M_{01}
\end{aligned} \tag{2.6}$$

With introducing the central moments in Eqs. 2.6, first important feature of central moments can be defined as translational invariant [13]. Translation invariant means that the moments are invariant to geometric shifts of the object in terms of shifting the coordinates of the origin of the object in the image [13]. In other words, the coordinates of the investigated object do not matter during the calculation of

Image Moments. The term '*invariant*' is the key feature of Image Moments which will be explained detailed later in this section.

$$\eta_{ij} = \frac{\mu_{ij}}{{\mu_{00}}^{(i+j)/2+1}} \tag{2.7}$$

Invariance to translation is not enough property to extract information from images so a new property, scaling invariance, is introduced with normalized central moments in 2.7. Scaling is done by dividing the central moments by the first central moment. By means of it, usage of first central moment is preferred because low-order moments are more stable to noise and easier to calculate [13]. Image moments become both scaling and translational invariant.

$$\begin{aligned}
I_1 &= \eta_{20} + \eta_{02} \\
I_2 &= (\eta_{20} - \eta_{02})^2 + 4{\eta_{11}}^2 \\
I_3 &= (\eta_{30} - 3\eta_{12})^2 + (3\eta_{21} - \eta_{03})^2 \\
I_4 &= (\eta_{30} + \eta_{12})^2 + (\eta_{21} + \eta_{03})^2 \\
I_5 &= (\eta_{30} - 3\eta_{12})(\eta_{30} + \eta_{12}) \left[(\eta_{30} - \eta_{12})^2 + 3(\eta_{21} + \eta_{03})^2\right] \\
&\quad + (3\eta_{21} - 3\eta_{03})(\eta_{21} + \eta_{03}) \left[3(\eta_{30} + \eta_{12})^2 - (\eta_{21} + \eta_{03})^2\right] \\
I_6 &= (\eta_{20} + \eta_{02}) \left[(\eta_{30} + \eta_{12})^2 - (\eta_{21} + \eta_{03})^2\right] + 4\eta_{11}(\eta_{30} + \eta_{12})(\eta_{21} + \eta_{03}) \\
I_7 &= (3\eta_{21} - \eta_{03})(\eta_{30} + \eta_{12}) \left[(\eta_{30} + \eta_{12})^2 - 3(\eta_{21} + \eta_{03})^2\right] \\
&\quad - (\eta_{30} - 3\eta_{12})(\eta_{21} + \eta_{03}) \left[3(\eta_{30} + \eta_{12})^2 - (\eta_{21} + \eta_{03})^2\right]
\end{aligned} \tag{2.8}$$

Eqs. 2.8 has an importance to introduce the final invariance property. These famous 7 equations also called Hu moments which were first introduced by Hu [14]. First 6 moments become translation, scale and rotation invariant as a result of all these operations [14].

id	Image	H[0]	H[1]	H[2]	H[3]	H[4]	H[5]	H[6]
K0	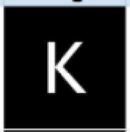	2.78871	6.50638	9.44249	9.84018	-19.593	-13.1205	19.6797
S0	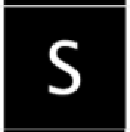	2.67431	5.77446	9.90311	11.0016	-21.4722	-14.1102	22.0012
S1	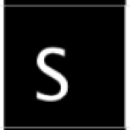	2.67431	5.77446	9.90311	11.0016	-21.4722	-14.1102	22.0012
S2	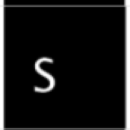	2.65884	5.7358	9.66822	10.7427	-20.9914	-13.8694	21.3202
S3		2.66083	5.745	9.80616	10.8859	-21.2468	-13.9653	21.8214
S4	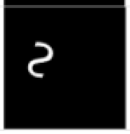	2.66083	5.745	9.80616	10.8859	-21.2468	-13.9653	-21.8214

Figure 2.4: Several Image Moment Calculation of Grey-Scale Images [16]

For example, Image Moments of letter K and S are calculated for different cases in Figure. There are differences between images with id K0 and S0, however, there almost no changes between images with ids S0 to S4. The only obvious change in Image Moments value is the H[6] value between image S3 and S4 because the last Hu Moment's sign changes when image reflection happens as it happened for H[6] value of the last image in the Figure 2.4. This is a great proof of how Hu Moments are translation, scale and rotation invariant because examples of rotated, translated and scaled images with same Hu Moment values exist in the Figure 2.4. Most important and most common usage of Image moments is to extract information from images which are invariant to scaling, rotation and translation. These all invariances are geometric transformations but there is also a non-geometric transformation called blur invariance. It is firstly introduced by Flusser and Suk[Flusser and Suk] in which how blur invariants are extracted from moment invariants. Since it is independent from blur, Flusser and Suk [17] proved the success of blur invariance on out-of-focus images and blurred face recognition images.

Meanwhile, Image Moments are local and global invariant too. For local invariance, a certain neighborhood around the object boundaries is considered but whole image is considered for the global invariance feature of Image Moments [13]. Last but not least, fast computation of Image Moments is ensured with the improved GPU power and fast computation algorithms in recent years [18].

Furthermore, Image Moments are mainly introduced for pattern recognition by Hu [14] but it is widely used for different purposes. Pattern recognition is possible with feature extraction and it is deeply tested by Barczak [19] to find a pattern for Handwritten Digits. Although it provides a significant successful result, Handwritten digits still have some ambiguity. Main advantage of using Image Moments is that it is a fast and easy to apply. Another similar application is performed by Fernando and Wijayanayake [20] for Real Time Sign Language Communication using visual data. The only limitation for that application is for similar hand shapes with different rotations/positions. Since Hu Moments are translation and rotation variant, values of Hu Moments with similar shape will be same in the case of rotation of hand demonstration for different letter representations. In order to solve this problem, a new easy feature is applied by [20] again which is height to width ratio. This intelligent feature eliminated the problem for problematic cases. Another interesting work is done by Rocha[Rocha] for object tracking and predicting the next move of an object. Obviously, pattern recognition tasks are located at the center of Image Moments. Image Moments are applicable with all types of Neural Networks defined in Section 2.2.1. Khan [15] used RNN for recognize situation using visual data coming from surveillance cameras. Image Moments are used in the work of Zhao [21] with a Feedforward Neural Network to predict the rotational angle of a camera frame with respect to the desired position of camera. Besides, CNN is the most used Neural Network type for image analysis, so it is not surprising that Image moments are also used with CNNs. Limitations of CNN tried to be eliminated in the work of AbuRass [22]. Beyond the translational, rotational and scale invariance features of Image Moments, CNNs are also translational invariant due to the fact that, CNN uses all the pixels of images by convolving all over the image to be able to extract the image's features [22]. Eventually, Image Moments helped to optimize CNN architecture by providing scale and rotation invariance features too. Image Moments(Hu Moments) are used as inputs of the Feedforward Neural Network to predict Non-Dimensional Apex Pressure and Non-Dimensional Gravitational Control Parameter in this project. These non-dimensional parameters are needed to calculate the Surface Tension of a Pendant Drop. These parameters and equations belong to these parameters will be explained in the next section.

2.4 Physics of Pendant Drop

2.4.1 Mathematical Equations

Main goal of the pendant drop tensiometry method is to measure interfacial tension of a drop. The physics behind pendant drop tensiometry and the mathematical equations are used and inspired by the work of Berry [1] and Kratz [2]. These mathematical equations expressed detailed because they are fundamental to create pendant drop images synthetically for this thesis work. These equations are also theoretical importance in order to better understand how and where they are used in previous pendant drop tensiometry techniques.

Bond Number

Bond number is based on the Young-Laplace equation and first termed by Bashfort and Adams [7] as β which is

$$\beta = \frac{\Delta\rho g {R_0}^2}{\gamma} \tag{2.9}$$

where $\Delta\rho$ is the density difference, g is the gravitational acceleration, R_0 is the drop dimension and γ is the interfacial tension. The parameter β was later named as Bond number by Merrington and Richardson [23] to honor Wilfred Bond due to finding the relation between terminal velocity and drops [24]. Bond number is calculated in to serve the main goal of this thesis because Bond number leads to the direct calculation of interfacial tension γ. Direct calculation is possible because density difference, gravitational acceleration and drop dimension are known quantities.

To start with, Young-Laplace equation is the relation between the curvature of the drop, interfacial tension and Laplace pressure as it is shown in Eq. 2.10:

$$\gamma\left(\frac{1}{R_1} + \frac{1}{R_2}\right) = \Delta P = \Delta \mathrm{P}_0 - \Delta\rho \mathrm{gz} \tag{2.10}$$

where R_1 and R_2 are the principal radii of curvature; ΔP is the Laplace pressure and $\Delta\rho = \rho_d - \rho$ is the density difference of the environment where drop belongs to. ρ_d is the drop phase density and ρ is the continuous phase density which are shown in Figure with other parameters of a pendant drop. Density difference can also be represented by other parameters such as reference pressure ΔP_0 and hydrostatic pressure $\Delta\rho g z$.

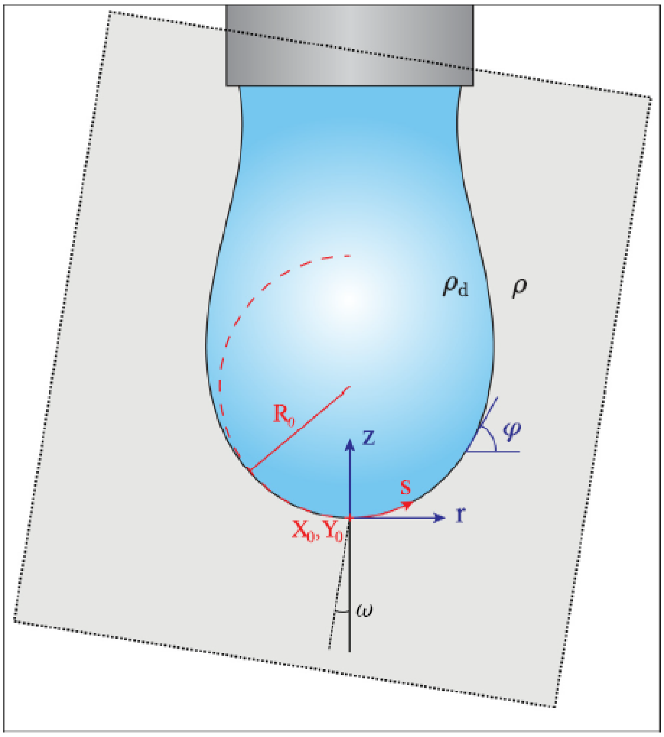

Figure 2.5: Pendant Drop Parameters According to Berry. Reprinted from [1], with the permission of Elsevier Publishing.

Since the pendant drop tensiometry method is defined as *Axisymmetric Drop Shape Analysis* (ADSA), Eq. 2.10 can also be represented by cylindrical coordinates [1] r, z and the tangent angle φ (see Figure 2.5). This transformation helps to write the Young-Laplace Equation with other dimensionless parameters to form new dimensionless differential equations [1] shown in Eq. 2.11:

$$\frac{d\varphi}{d\bar{s}} = 2 - Bo\ \bar{z} - \frac{\sin\varphi}{\bar{r}} \tag{2.11}$$

$$\frac{d\bar{r}}{d\bar{s}} = \cos\varphi \tag{2.12}$$

$$\frac{d\bar{z}}{d\bar{s}} = \sin\varphi \tag{2.13}$$

where the dimensionless parameters are expressed with using a bar above them. Berry [1] created dimensionless parameters scaling them by R_0 which is the radius of curvature at the drop apex.

$$\bar{r} = r/R_0, \quad \bar{z} = z/R_0, \quad \bar{s} = s/R_0 \tag{2.14}$$

All the parameters can be obviously in Figure 2.5. Differential equations with dimensionless parameters are introduced because Young-Laplace equation can be only solved for sphere droplet shapes which is the trivial case. By means of it, this leads to an irrational solution for pendant drop tensiometry because it tends to $\gamma \rightarrow \infty$ [1].

In Eq. 2.11, Bo represents the Bond number which is same with Eq. 2.9:

$$Bo = \frac{\Delta\rho g {R_0}^2}{\gamma} \tag{2.15}$$

Eq. 2.15 is valid for boundary conditions presented as:

$$\bar{r} = 0, \quad \bar{z} = 0, \quad \varphi = 0 \quad at \quad \bar{s} = 0. \tag{2.16}$$

If R_0 and Bond number can be extracted from the captured image of a pendant drop, γ can be directly calculated since $\Delta\rho$ and g are already known. This is exactly the fundamental behind the pendant drop tensiometry technique to obtain the interfacial tension γ.

Non-Dimensional Apex Pressure and Non-Dimensional Gravitational Control Parameter

After evaluating the perspective of Berry [1] in previous section Kratz presented a new perspective by introducing non-dimensional parameters. Again differential equations are presented but Kratz uses Ψ, the angle of the drop normal with the z-axis which is illustrated in Figure and means that cylindrical coordinates are used by Kratz again [2].

$$\frac{dr}{ds} = \cos\Psi \tag{2.17}$$

$$\frac{dz}{ds} = \sin\Psi \tag{2.18}$$

All the equations presented in previous section are valid also for this section too but there is an additional boundary condition presented by Kratz [2]:

$$r = a/2 \text{ at } s = L \tag{2.19}$$

where L stands for the total length of arc. This additional boundary condition is for presenting the attachment to the capillary [2]. Another new parameter are principal curvatures which are circumferential curvature K_ϕ and meridional curvature K_S. This parametrization is illustrated together with other parameters detailed in Figure. Before Berry obtained the dimensionless parameters scaling them by R_0 but Kratz scaled them by a which is the capillary diameter.

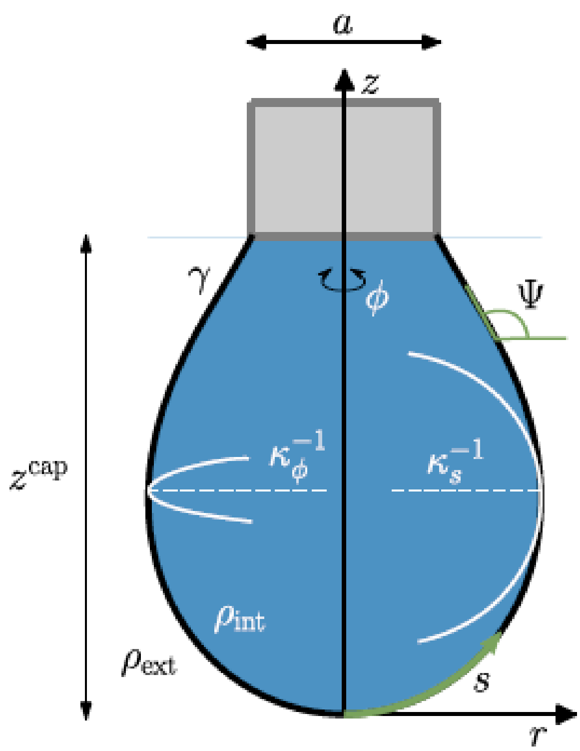

Figure 2.6: Pendant Drop Parameters According to Kratz. Reprinted from [2], with the permission of AIP Publishing.

$$\widetilde{r} = r/a, \quad \widetilde{z} = z/a, \quad \widetilde{s} = s/a, \quad \widetilde{K}_{S,\phi} = K_{S,\phi} * a \tag{2.20}$$

After some derivations, Kratz [2] presented the Young-Laplace equation as following:

$$p_L - \Delta\rho g z = \gamma(K_\phi + K_S) \tag{2.21}$$

$K_\phi = K_S$ condition at the apex is derived by using the advantage of axisymmetry and the apex Laplace pressure p_L is related with the radius of curvature R_0 in the apex as following:

$$p_L \;=\; 2\gamma/R_0 \tag{2.22}$$

The apex Laplace pressure p_L is the same parameter which is introduced in the previous section as ΔP_0 in the Eq. 2.10. After this point, the parameter will be considered as p_L and will be called as "apex pressure".

Kratz [2] inserted K_S and K_ϕ into Eq. 2.21 and derived another form of Eq. 2.10 using together with Eq. 2.22:

$$\frac{d\Psi}{ds} = \frac{p_L}{\gamma} - \frac{\delta\rho g z}{\gamma} - \frac{\sin\Psi}{r} \tag{2.23}$$

Eq. 2.23 will be further useful for the Python code for synthetic drop image generation and will be explained detailed how it is used to generate drop shapes.

Finally, creating non-dimensional parameters are the most critical part of presenting these equations which will be further explained in the Chapter 3. Using Eq. 2.20 Kratz [2] created non-dimensional Young-Laplace equation, non-dimensional apex pressure $\widetilde{p}_L$ and non-dimensional gravitation control parameter which are presented as following:

$$\widetilde{p}_L - \Delta\widetilde{\rho}\widetilde{z} = \widetilde{K_\phi} + \widetilde{K_S} \tag{2.24}$$

$$\widetilde{p}_L = \frac{p_L a}{\gamma} \text{ and } \Delta\widetilde{\rho} = \frac{p_L a}{\gamma} \tag{2.25}$$

The main objective of Kratz [2] is predicting $\widetilde{p}_L$ and $\Delta\widetilde{\rho}$ parameters with using Neural Networks algorithm. These two parameters are the parameters which are predicted by Neural Networks in this thesis work too but, they are predicted using a completely different way and different architecture. One last thing about Bond number is introduced by Kratz [2]. Previously Berry [1] proved that if R_0 and Bond number can be obtained, interfacial tension γ can be obtained directly too. For this purpose, a relation is found between apex pressure p_L, gravitational control parameter $\Delta\rho$ and Bond number Bo. Combining Eq. 2.22 and Eq. 2.15 Bond number becomes:

$$Bo = \frac{\Delta\rho g \gamma}{{p_L}^2} \tag{2.26}$$

Since calculating Bo and R_0 was enough to calculate interfacial tension γ, calculating p_L and $\Delta\rho$ can be also another tool for calculating interfacial tension so as their non-dimensional versions. These are all derivations that is done by previous works, however, further derivations also done in this thesis work which will be explained in Chapter 3. This section aimed to explain the principle behind extracting the non-dimensional parameters which will be the output of the Neural Network of this project.

Non-dimensional gravitational control parameter is more critical parameter than non-dimensional apex pressure. When apex pressure $\widetilde{p}_L$ cannot be obtained in any experiment, interfacial tension γ must be extracted from $\Delta\widetilde{\rho}$ [2]. This is possible because density difference between environment and drop $\Delta\rho$, and capillary diameter a are known parameters.

2.4.2 Shape Factor(Number of Events)

Pendant drops have different profiles under non-dimensional parameters but, non-dimensional parameters are not always enough to determine drop characteristics. 'Number of events' term is presented in order to help inferring situational analysis of drop shapes. Drop profiles have several maxima (bulges) and several minima (necks) values even if the solution of the Young-Laplace equation leads to the same solution [2]. This means that a drop can have different profiles for the same $\widetilde{p}_L$ and $\Delta\widetilde{\rho}$ value. Different profiles of drops for same solution will be further explained and exampled in Section 3.2. Number of events parameter is named as "shape factor" by Kratz [2] and represented as:

$$\Omega = 1 + \#\text{necks} + \#\text{bulges} \tag{2.27}$$

In this thesis, 3 conditions are observed in which $\Omega = 1$, $\Omega = 2$ and $\Omega = 3$. Drop shapes which have $\Omega > 3$ are not considered due to the fact that, these conditions are unstable, unstable and very rare to occur [2]. Figure 2.7 represents three examples of drop shapes that are more likely to occur. Blue drop profile has $\Omega = 1$, orange drop profile has $\Omega = 2$ and green drop profile has $\Omega = 3$. Figure 2.8 represents a synthetically generated drop shape with $\Omega = 3$ and *bifurication lines*.

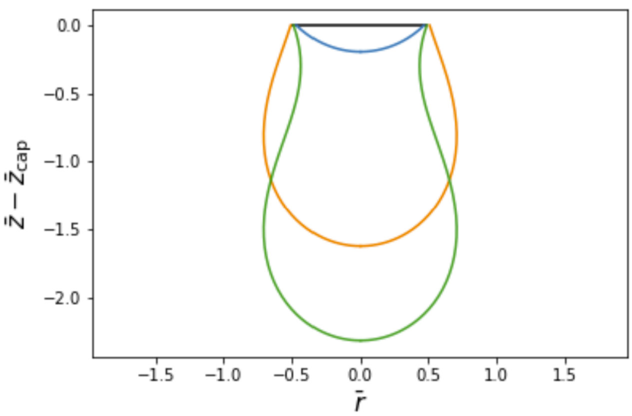

Figure 2.7: Different Drop Profiles According to Number of Events ($\Omega = 1$, $\Omega = 2$, $\Omega = 3$)

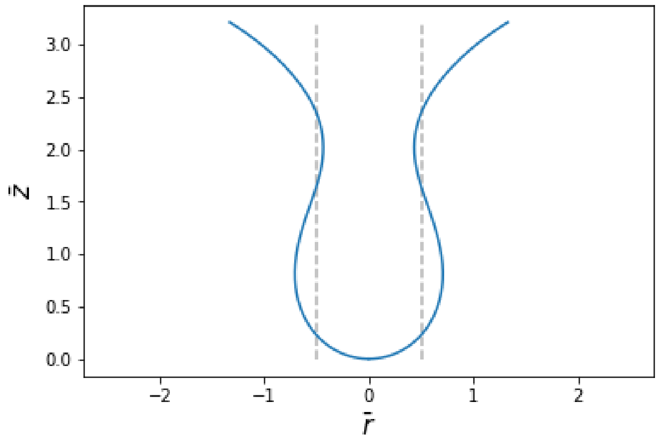

Figure 2.8: Example of Drop Profile with Bifurication Lines

Vertical lines-*Bifurication Lines*- are to show the capillary width and how many times the contour of drop crossed the bifurication lines should be observed to determine the number of events. In other words, $\Omega = 3$ is a non-convex condition and sum of number of necks and number of bulges are equal to 2 where there is only 1 bulge and 1 neck. The neck is at the capillary and the neck also crosses the capillary boundary(see Eq. 2.19) [2]. This is the trivial logic behind the number of events.

Solution for $\Omega = 2$, results in convex shapes and has exactly one bulge without a neck. Bulge is wider than capillary and if you image vertical lines of capillary, drop contour crosses 2 times. Final solution for $\Omega = 1$, results in simple convex shape as it is the most left case in Figure 2.7.

To sum up, cut off points in bifurication lines, necks and bulges are important to determine the drop profile. This metric is very useful while creating the synthetic image of a pendant drop which will be explained in Chapter 3.

2.4.3 Previous Pendant Drop Approaches

In this section some of the pendant drop techniques will be introduced. After observing all previous works, it can be obviously seen that there is a gap in this area and this thesis work is implemented to full this gap. There is only a single approach that is related with Machine Learning which is done by Kratz [2].

First of all, Berry provided a fitting of Young-Laplace equation to an experimental image which demands a high-level computational routine [1] in 2015. Method is divided into two steps. First step is to extract the experimental image from a camera. Then, Young-Laplace equation is iteratively solved to find optimized parameters which are expressed in Section 3.2. During the process, image analysis techniques are used such as Canny edge detector to determine the drop profile with its optimal physical parameters such as surface tension γ. An initial drop profile is presented and then, iterative application of Young-Laplace equation with edge detection algorithms applied in order to make the initial guess converge to the true drop profile. Fitting the profile to the true profile is done by minimizing the some of squared residuals like Euclidian distance between guess and true drop contour. Berry reached to an standard error approximately 1%. Cabrerizo-Vilchez [25] provided a new solution method integrated with pendant drop tensiometry in 2019. Most of the work follows the equations and physical parameters such as Young-Laplace equation introduced in section 2.4.1. Sessile drops and captive bubbles are observed beyond pendant drop and pendant bubble by adding a new mathematical point of view to pendant drop approach. Well-known Newton method applied to Young-Laplace equation to fix the volume of a drop as well as its position in the capillary [25]. Experimental bubbles are used together with MATLAB codes to determine surface tension. After validating experimental results with theoretical values, less than 1% relative error is obtained. Busoni and Carlà [26] provided one of the fastest algorithm in the literature for determining the surface tension using the ASDA measurement. On the other hand, the algorithm is implemented only for sessile drops so, they are not valid for pendant drop profiles. It has still not implemented using a Machine Learning approach but it could be evaluated as successful in terms of speed. Charged Coupled Device (CCD) solid state camera is used and the experimental apparatus is much complicated than other works that are observed in this thesis work. Algorithm is tested with images has frame size 1024x1024 by applying some blurring to images. Then the results are compared according to different noise levels and less than 1% error is obtained. Ferrera [27] provided a comparison between two techniques which are pendant drop tensiometry and liquid bridges. Comparison was made in terms of sensitivity and Ferrera proved that pendant drop method was not much sensitive to very small changes in drop shape profiles. This thesis work also tried to eliminate this insensitivity to very small changes. Insensitivity was observed over the Bond number parameter and using synthetic images which also one of the common points between this thesis and Ferrera's work. Greyscale images are analyzed and 1024x1024 pixel images were obtained through CCD cameras. Even if liquid bridges were proved to be more sensitive than pendant drop technique, pendant drop technique still recommended due to having a simpler setup [27]. Less than 1% relative absolute error was obtained for pendant drops which had very small volume approximately 10mm3. Consequently, the only work which includes a Machine Learning approach was presented by Kratz [2]. Kratz presented all the equations that are presented in Section 2.4.1 and introduced non-dimensional apex pressure $\widetilde{p}_L$ and non-dimensional gravitational control parameter $\Delta\widetilde{\rho}$. Pendant drops were created synthetically but there are not any records about the resolution. Kratz mentioned some imperfections could arise because of limited camera resolution [2]. A Neural Network architecture was built to predict $\widetilde{p}_L$ and $\Delta\widetilde{\rho}$ using cylindrical coordinates $\bar{r}$ and $\bar{z}$ to calculate interfacial tension γ. Additionally, Conventional Shape Fitting (CSF) algorithm also applied to compare its results with the Machine Learning approach. A graph for valid pendant drop shapes was provided and validity is in terms of number of events. This graph has a very important role in this thesis work which will be explained in Section 3.2 about how it is used in thesis work. The training took approximately 3 weeks because model was trained for 90, 000 epochs and each epoch contains 0.5 million drop shapes. Test set was formed by 0.9 million drop shapes and MSE was found as $2.10^{-}7$. Performance of the Deep Neural Network was recorded better than CSF algorithm and both algorithms are more successful while predicting $\widetilde{p}_L$. CSF generally were good at predicting well-conditioned drop profiles, however, Machine Learning approach were good at both ill-conditioned and well-conditioned drop shapes [2]. This thesis brings an innovative and simpler solution to Kratz's work by introducing Image moments and simpler Neural Network architecture.

Chapter 3

Proposed Methodology

This approach is based on a step-by-step algorithm and a sequential work is followed during the implementation of thesis:

1. **Mathematical Model Derivation:** So many mathematical equations are presented in Section 2342 and these are used to derive a final Young-Laplace equation to generate synthetic drop shapes. Main equations are based on Bond number. Thanks to Kratz's [2] derivations, Young-Laplace equation and Young-Laplace related differential equations can be also based on non-dimensional parameters $\widetilde{p}_L$ and $\Delta\widetilde{\rho}$. New Young-Laplace equation is provided in this thesis work to artificially generate pendant drop shapes in order to prepare a dataset.

2. **Dataset Preparation:** After setting all the equations for generating drop shapes, Many $\widetilde{p}_L$ and $\Delta\widetilde{\rho}$ values are gathered from a graph which is introduced valid according to number of events by Kratz [2]. From gathered non-dimensional parameters, synthetic pendant drop images are generated. Then, Image Moments are calculated from drop images which are recorded as features to make them ready for feeding the Neural Networks.

3. **A Machine Learning Approach (Neural Networks):** As it is mentioned before, surface tension parameter γ is the parameter that is predicted indirectly by the Machine Learning algorithm. Deep Learning model is built to predict non-dimensional apex pressure $\widetilde{p}_L$ and non-dimensional gravitational control parameter $\Delta\widetilde{\rho}$. Deep Neural Network is fed with a dataset which is created synthetically. Features of the Neural Networks are Image Moments computed from synthetically generated different pendant drop shapes with the help of OpenCV [16] library of Python. Labels which are going to be regressed by the Neural Network are the non-dimensional parameters $\widetilde{p}_L$ and $\Delta\widetilde{\rho}$.

3.1 Mathematical Model Derivation

Young-Laplace equation stands in the heart of determining surface tension of a pendant drop. It was first presented as it is presented in Eq. 2.10 and further detailed with differential equations using Bond number in Eq. 2.11. Kratz [2] derived differential equations with p_L and $\Delta\rho$ expressed as in Eq. 2.17, 2.18 and 2.23. At the final stage of Kratz's work non-dimensional versions of p_L and $\Delta\rho$ expressed as $\widetilde{p}_L$ and $\Delta\widetilde{\rho}$ but there aren't any differential equation derivations with using non-dimensional parameters $\widetilde{p}_L$ and $\Delta\widetilde{\rho}$. Since $\widetilde{p}_L$ and $\Delta\widetilde{\rho}$ are used to generate synthetic drop shapes, a differential equation which includes these parameters should be derived. This thesis brings an innovation at this point and derived a new differential equation Eq. 3.1:

$$\frac{d\Psi}{d\widetilde{s}} = \widetilde{p}_L - \Delta\widetilde{\rho}\,\widetilde{z} - \frac{\sin\Psi}{\widetilde{r}} \tag{3.1}$$

All these derivations are done for a purpose: to calculate surface tension γ via Bond number. For this purpose, a relation should be found between Bond number and non-dimensional parameters $\widetilde{p}_L$ and $\Delta\widetilde{\rho}$. This relation is also extracted from equations that are presented by Kratz [2]. The derivation process starts with inserting Eq. 2.22 to Eq. 2.15 and continues with inserting Eq. 2.25 to obtain:

$$Bo = \frac{4\Delta\widetilde{\rho}}{\widetilde{p}_L} \tag{3.2}$$

3.2 As it is described in Section 2.4.1, surface tension can be calculated using Bond number Bo and apex radius R_0. Since $\widetilde{p}_L$ and $\Delta\widetilde{\rho}$ are predicted in this thesis, Eq. 3.2 is derived to achieve surface tension. Next step is to calculate apex radius R_0 which is derived combining 2.22 and 2.25:

$$R_0 = \frac{2a}{\widetilde{p}_L} \tag{3.3}$$

Berry [1] was using R_0 to pass dimensionless space but Kratz [2] was using capillary diameter a to pass dimensionless space. These equations makes possible to work with all parameters. Now, all the equations and parameters, that will be used to generate synthetic images, are presented. It is time to pass how images are created and how the dataset is prepared.

3.2 Dataset Preparation

This section is observed under three subsections: *Gathering Non-Dimensional Parameters, Binary Image Generation, Image Moments Calculation.* The process followed to generate dataset will be explained.

3.2.1 Gathering Non-Dimensional Parameters

After finishing the derivation process of all the equations, non-dimensional apex pressure $\tilde{p}_L$ and non-dimensional gravitational control parameter $\Delta\tilde{\rho}$ are used to generate synthetic pendant drop images. These parameters are extracted from a graph which is published in the Kratz's work [2]. As it is also explained in Section 2.4.2, there are likely and unlikely pendant drop profiles that can occur. According to $\tilde{p}_L$ and $\Delta\tilde{\rho}$ values drop profiles differ and a graph is constructed with regions to Show this differentiation by Kratz [2]. This graph is divided into regions and regions for pendant drop profiles, which are likely to occur, named as "*Valid Regions*" in this project. $\tilde{p}_L$ and $\Delta\tilde{\rho}$ values are extracted from Valid Regions to use them to generate favorable drop shapes. The Figure 3.1 taken by Kratz's work and we marked valid regions with green and unused regions are marked as red in Figure 3.2 to show the separation clearly.

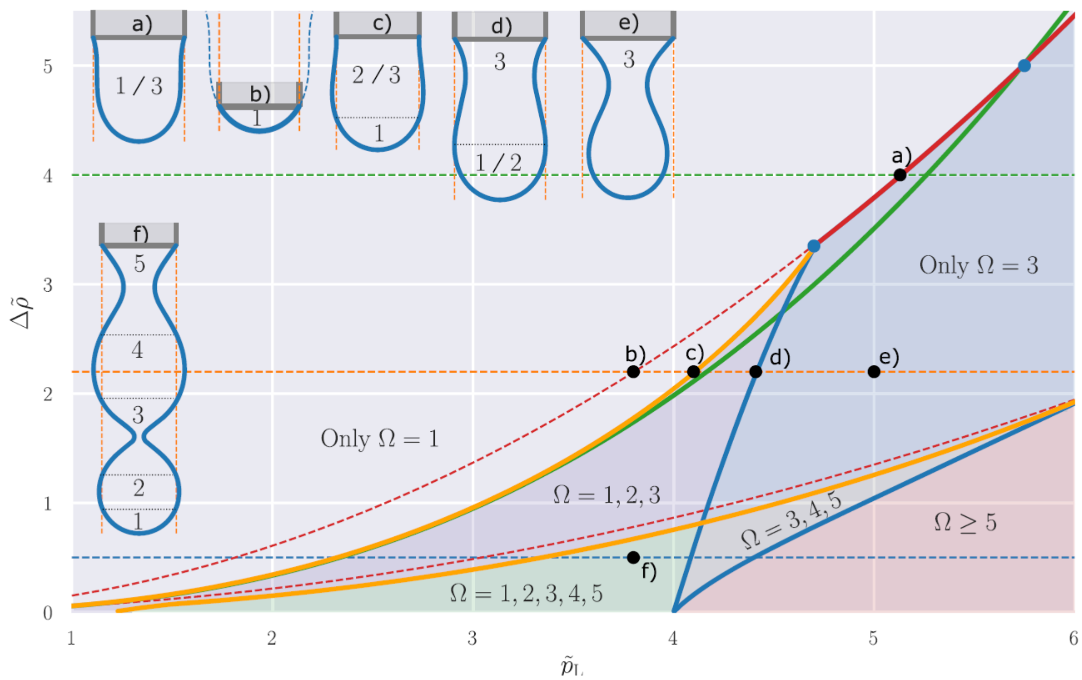

Figure 3.1: Graph of Valid Regions According to Number Shape Factor Ω. Reprinted from [2], with the permission of AIP Publishing.

In the Section 2.4.2, shape factor Ω = 2,3 conditions are considered so green marks are placed according to that condition. We also marked the curves which encloses and separates the valid regions. By marking curves with red in Figure 3.2, we tried to digitize this graph to extract the points on curves to draw these curves in Python. This digitization was done by using a web plot digitizer tool [28]. After extracting the points to a *csv* file, interpolation functions are applied on Python to plot these curves digitally. This digitization is one of the key factors in this thesis to generate synthetic dataset. Digitized form of graph is illustrated in Figure 3.2.

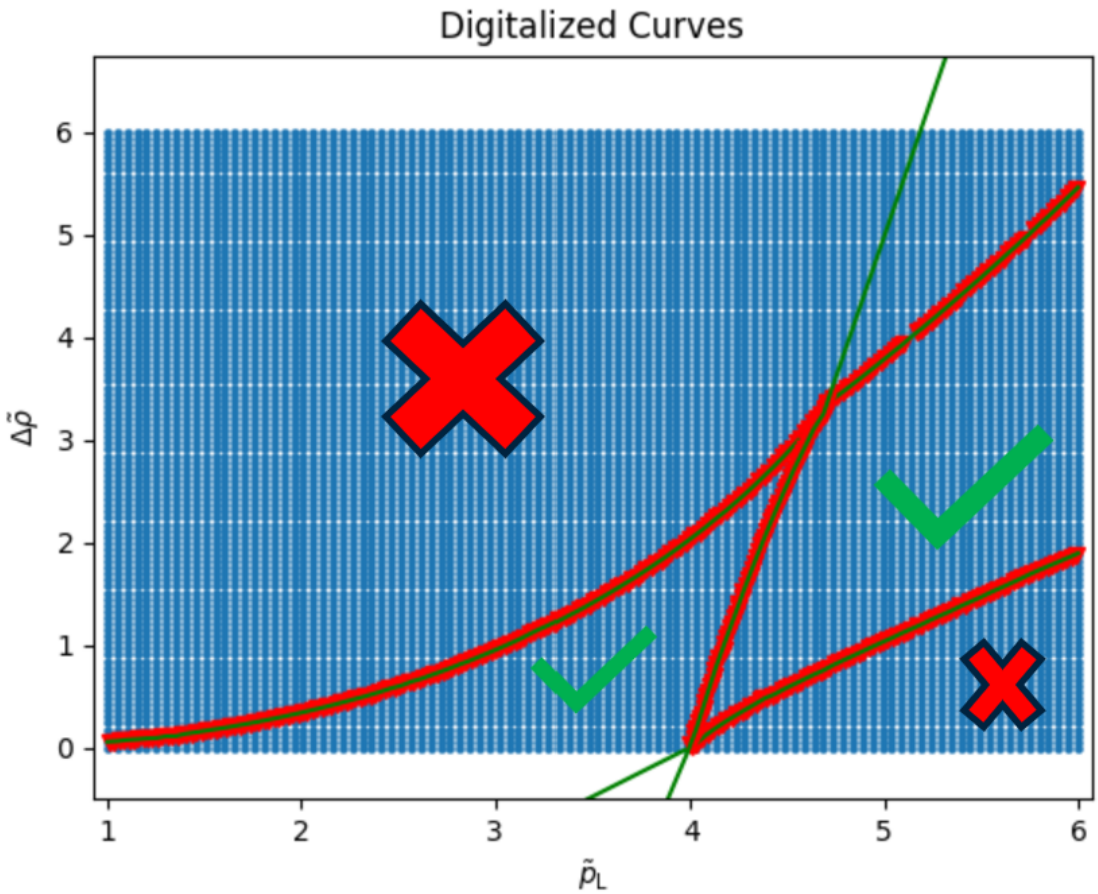

Figure 3.2: Digitized Valid Regions on Python According to Number Shape Factor Ω

Valid Regions are marked with green again to show the separation clearly. Points are generated by sampling and Valid Regions are also divided into two. There are two different valid regions according to pendant drop profiles which have different number of events.

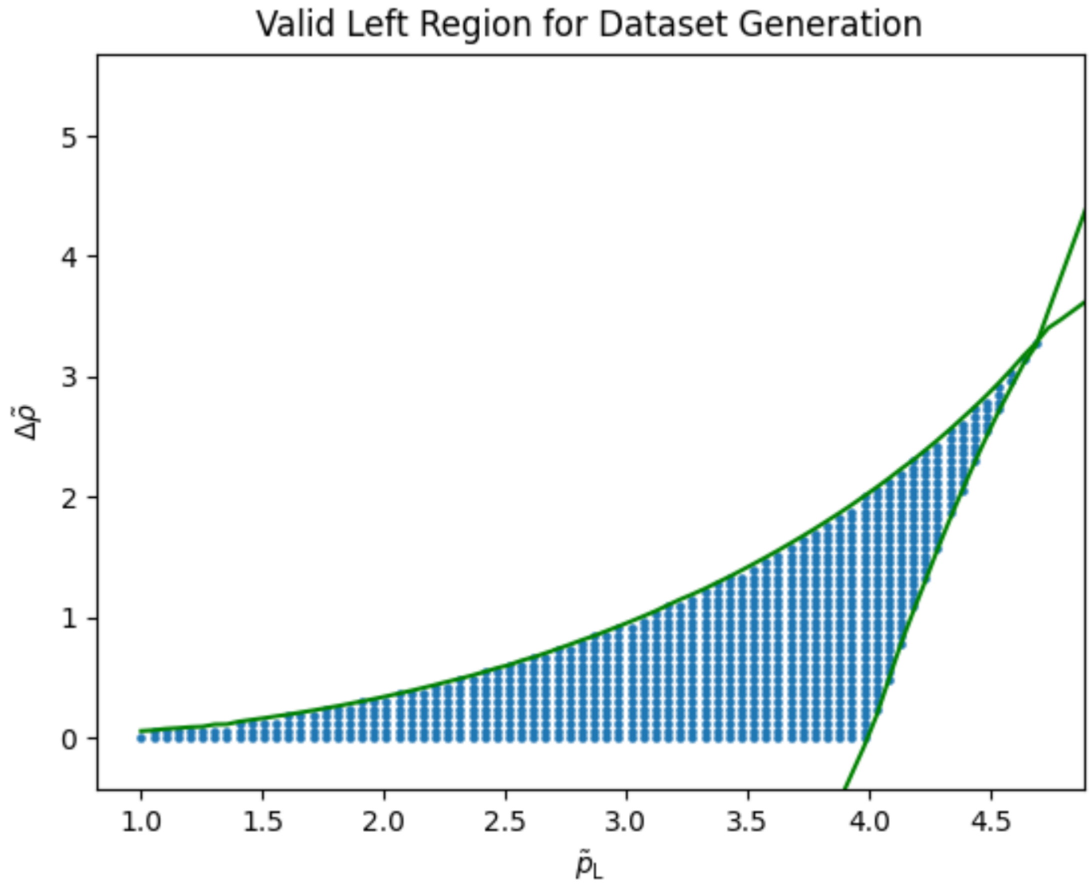

Figure 3.3: Digitized Valid Left Regions on Python According to Number Shape Factor

Figure 3.3 shows *Valid Left Region* which includes drop profiles for two different number of event values ($\Omega = 2$ and $\Omega = 3$). Valid Left Region has 863 samples but Left Region data is used twice for different number of events($\Omega = 2$ and $\Omega = 3$) so, size of the Valid Left Region could be considered as 1726 samples.

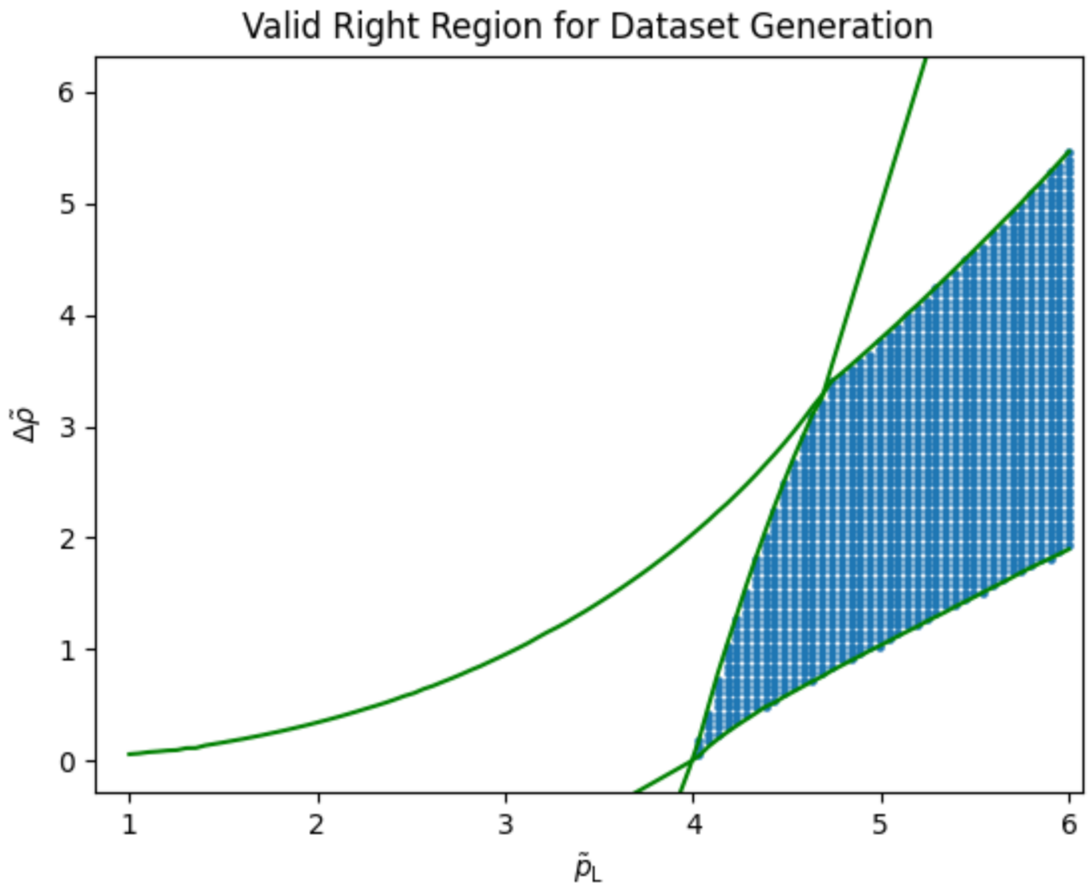

Figure 3.4: Digitized Valid Right Regions on Python According to Number Shape Factor Ω

Figure 3.4 shows the *Right Valid Region* which includes drop profiles for only $\Omega = 3$ and Right Valid Region has 1630 samples. Total Data that is used for Neural Network becomes 3356.

3.2.2 Binary Image Generation

When the extraction process of $\tilde{p}_L$ and $\Delta\tilde{\rho}$ values are finished, these values are used to create binary synthetic pendant drop images. Mathematical derivations also helped to generate these images because differential equations 2.17, 2.18 and 3.1 are solved using *Ordinary Differential Equations* (ODE) Solver called "Runge-Kutta (RK45)" Method. This is provided by scikit-learn library [29] in Python. RK45 is a method of order 5, have a 'small' principal truncation term in the fifth order [30] and provides a rapid and accurate solution [2]. Derived differential equations are solved according to initial conditions which are determined according to boundary conditions in equations 2.14 and 2.19. ODE solver iteratively solves these differential equations according to number of event values. For instance, if $\Omega = 2$, differential equations are solved two times by the ODE solver.

As a result of the solution, a symmetric half of the pendant drop is generated. Full pendant drop shape is generated by flipping the symmetric half. The advantage of being an axisymmetric drop shape analysis is used in this case.

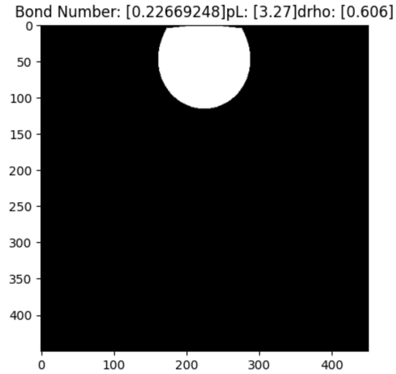

Figure 3.5: Synthetic Pendant Drop Shape Example from Left Valid Region($\Omega = 2$)

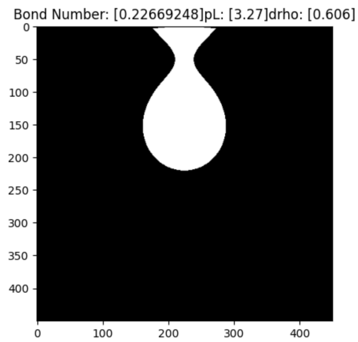

Figure 3.6: Synthetic Pendant Drop Shape Example from Left Valid Region($\Omega = 3$)

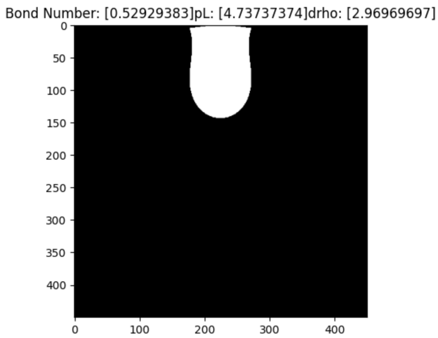

Figure 3.7: Synthetic Pendant Drop Shape Example from Right Valid Region($\Omega = 3$)

In the previous section it is explained that, two different drop profiles are generated according to different number of event values. Figure 3.5 and 3.6 are the example of different shapes for same Bo, $\widetilde{p}_L$ and $\Delta\widetilde{\rho}$ values. Even if two pendant drops have the same Bo, $\widetilde{p}_L$, $\Delta\widetilde{\rho}$ and surface tension γ, they can have different profiles. That's why the Left Valid Region data is used twice.

Finally, Figure 3.7 is an example from Right Valid Region whose $Bo \approx 0.53$,

$\widetilde{p}_L \approx 4.73$, $\Delta\widetilde{\rho} \approx 2.97$ and $\Omega = 3$. The next step is to calculate image moments from these gray-scale images in order to finalize the dataset.

One limitation arises at this point in terms of image resolution because all the images are generated with $500x500$ image size. Eventually, training process includes only images which has only $500x500$ size. Image Moments are stabilized after an approximate image resolution of $150x150$ which is proved by Huang and Leng [31]. According to Huang's work [31], image resolution will not be a problem for images whose resolutions are more than $150x150$ but still this could a limitation to be tested.

Another problem arises in the shapes of synthetic pendant drops. Although images are almost same to the real images, there are very small gaps at the most top of the images. White pixels should cover more place at the very top in order to be equal to the capillary diameter of the tube. After some rows the width of the drop becomes equal to capillary diameter however, it should be equal directly at the first row. This problem is caused by *polygon* function in python due to create more "pixeled" shapes at the edges. A more precise model is introduced by Mizotin [32] which eliminates the difference between synthetic images and real images by reducing the error while creating synthetic drop shapes.

3.2.3 Image Moments Calculation

After generating synthetic drop images, Image Moments-Hu Moments- are calculated. There are 7 moments but the last one is not included in the dataset which represents the reflection symmetry. Since pendant drop tensiometry is ASDA, there is no need to use last Hu Moment property. Image Moments are very helpful in terms of creating a robust system because they are translation, scaling and rotation invariant. By using these properties the system becomes robust for rotated drop shapes, scaled drop shapes and translated drop shapes. These variety of conditions could differ according to the experimental setup that is created in a project.

One of the most critical application during calculating Hu Moments is the log scaling. Without using log scaling Hu Moment values are approximately between to 10^-7 and 10^-20 scales.

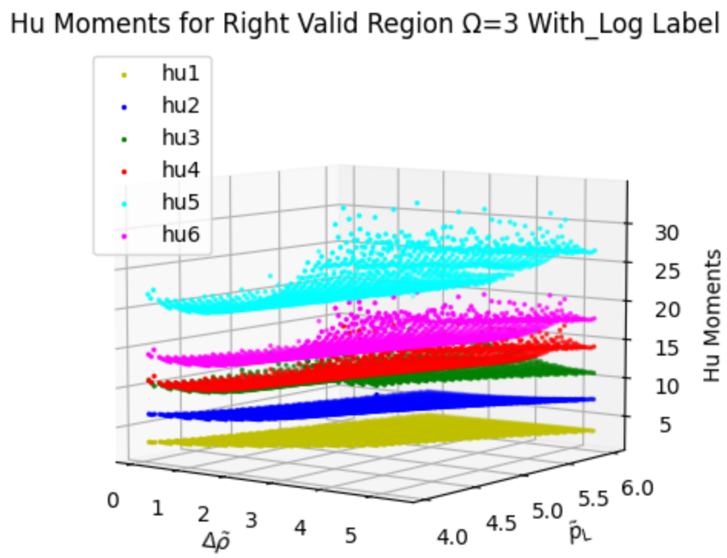

Figure 3.8: Hu Moments According to $\widetilde{p}_L$ and $\Delta\widetilde{\rho}$ for Right Valid Region($\Omega = 3$) With Log Operator

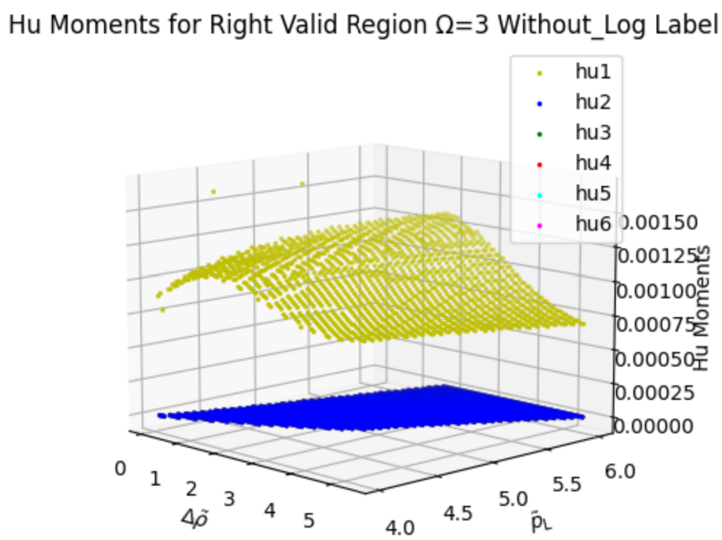

Figure 3.9: Hu Moments According to $\widetilde{p}_L$ and $\Delta\widetilde{\rho}$ for Right Valid Region($\Omega = 3$) Without Log Operator

In Figure 3.9, changes of Hu Moments with respect to $\widetilde{p}_L$ and $\Delta\widetilde{\rho}$ without applying a log scaling. All the five moments except first are same and varies in very low scale. All the moments except first and second seems like disappeared in

Figure 3.9 because they are almost same and 3D graph cannot illustrate all points. It can be interpreted as it is constant. On the other hand, Figure 3.8 shows the Hu Moment values using a log scaling and changes can be seen clearly so the Eq. 3.4 [16]

$$H_i = -\text{sign}(h_i)\log_{10}(h_i) \tag{3.4}$$

is applied where h_i is the calculated Hu Moments. After extracting(digitizing) the $\widetilde{p}_L$ and $\Delta\widetilde{\rho}$ values from graph and calculating Hu Moments, the dataset is ready. A *csv* file is generated using these parameters to feed the Neural Network.

3.3 A Machine Learning Approach (Neural Networks)

A simple Neural Network architecture is built to predict each non-dimensional parameter separately. In other words, we predict each parameter in separate Neural Networks, however, architecture of both Neural Networks is the same as for both predicting $\widetilde{p}_L$ and $\Delta\widetilde{\rho}$. The architecture is shown in Figure 3.10 and the summary of the model is shown in Figure 3.11.

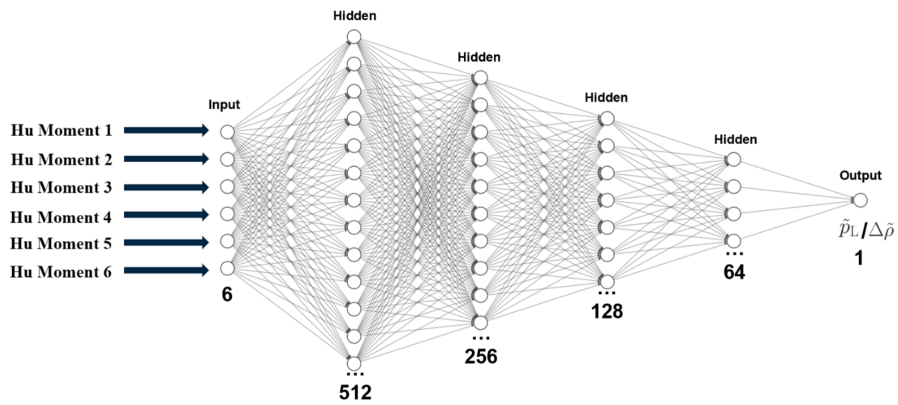

Figure 3.10: Neural Network Architecture

Model is decided according to some tests. Layer numbers are increased progressively to obtain the most successful architecture. For each validation of layer number, number of neurons progressively increased too. When the accuracy started not to improve, number of layers and neurons are recorded to finalize the validation phase to build most accurate Neural Network architecture.

There are 6 features(6 Hu Moments) to feed the Neural Network and the Network is constructed from 6 layers. Network has 1 input, 4 hidden and 1 output layer.

Since we have 6 features, input layer has 6 neurons and since we predict just one non-dimensional parameter for training. These non-dimensional parameters could be predicted in separate training phases because Kratz [2] proved that these non-dimensional parameters are independent. Training phase is done separately in parallel while running the algorithm. Model summary in Figure 3.11 represents how many layers are used with corresponding number of parameters.

```
Model: "sequential"
_________________________________________________________________
 Layer (type)                Output Shape              Param #
=================================================================
 dense (Dense)               (None, None, 512)         3584

 dense_1 (Dense)             (None, None, 256)         131328

 dense_2 (Dense)             (None, None, 128)         32896

 dense_3 (Dense)             (None, None, 64)          8256

 dense_4 (Dense)             (None, None, 1)           65

=================================================================
Total params: 176,129
Trainable params: 176,129
Non-trainable params: 0
```

Figure 3.11: Model Summary

A sequential model of Tensorflow Keras is used to train the Neural Network. Tensorflow is an open-source library by Google and tensor is a multidimensional array. Dataset is converted to tensor form before training and test process. 20% the dataset is used as Test set which corresponds to 672 data so the training is done using 2684 data. Before training and test each dataset is shuffled. This sequential model is compiled with using Adam Optimizer and loss metric is decided as Mean Square Error. Activation Function is decided as RELU and the decision process will be explained by results in the Chapter 4.

Chapter 4

Experimental Results

In this chapter, experimental results of the thesis will be analyzed with using numerical results. These results are obtained using different datasets which have different sizes. Results are tested for different activation functions, epochs and cross validation techniques. Moreover, results are supported and further explained with different statistical measures to reflect how the hyphothesis is verified or not. During evaluating the results, it is also investigated that, for which parts this thesis work brings an improvement and innovative solutions compare to previous solutions.

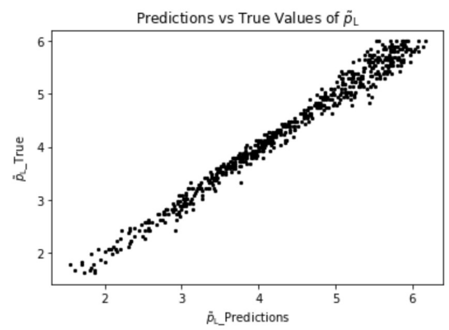

Figure 4.1: Predictions vs True Values of $\widetilde{p}_L$

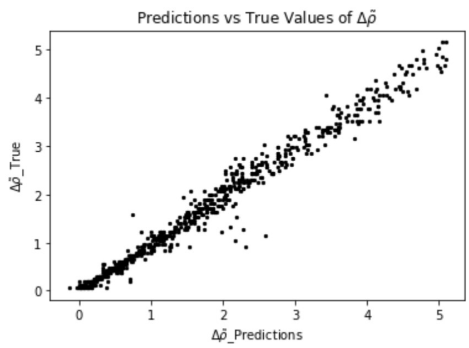

Figure 4.2: Predictions vs True Values of $\Delta\widetilde{\rho}$

We have validated the results using different statistical measures and graphs. Firstly, a scatter plot is used to verify the predictions. The expectation was to obtain $x = y$ graph since the predictions should be same with the true values of what we are trying to predict. Figure 4.1 and 4.2 is the first prove that our model is working successfully for the dataset because we almost obtain the $x = y$ graph. Figure 4.1 shows the predictions vs true values of $\widetilde{p}_L$ and Figure 4.2 shows the predictions vs true values of $\Delta\widetilde{\rho}$.

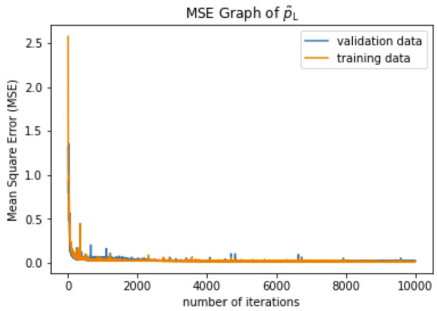

Figure 4.3: Mean Square Error of $\widetilde{p}_L$ vs Epochs

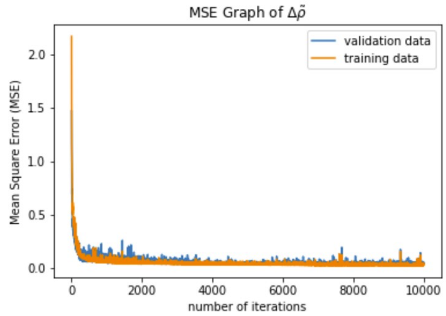

Figure 4.4: Mean Square Error of $\Delta\widetilde{\rho}$ vs Epochs

For the loss metric of the Neural Network, Mean Square Error (MSE) is considered to observe the decreasing error. The idea behind observing the MSE is to where to stop the training process and to see whether the Network saturates for a reasonable low error or not. Training process is done for 2684 data with 10000 epochs for each prediction process. Each training took approximately 2 hours in separate since we predict the non-dimensional parameters in different networks. The main objective of this thesis is provide an alternative(more simple and innovative) solution for pendant drop tensiometry using a Machine Learning approach together with Image Moments. Since we seek a more simple solutions we need to provide a less complex and rapid Machine Learning algorithm. As it is mentioned before, the only work using a Machine Learning approach is Kratz [2] and their training took approximately 3 weeks on a standard hardware(i3-CPU with a GTX 970 GPU). Meanwhile, training is done using standard Google Colab version in this thesis work and training took total 4 hours. In terms of being less complex, this thesis succeed in for this part of the hypothesis. This could be even decreased by applying an *early stopping*. Even if the error decreased a little after epoch 8000, there is no significant error decrease so the training could be stopped around epoch 8000 if a less precise result is enough.

In addition to this, there is no overfitting problem in the network model which could be obviously observed from Figure 4.3 and 4.4. *Overfitting* can happen when the test accuracy is low and the training accuracy is high. Orange curves in Figures 4.3 and 4.4 represents the training MSE loss and the blue curves represents the test MSE loss. Test MSE loss is little higher than training MSE loss as it is expected. Since both of the curves are very close to zero and converging to zero, there is no overfitting in the model.

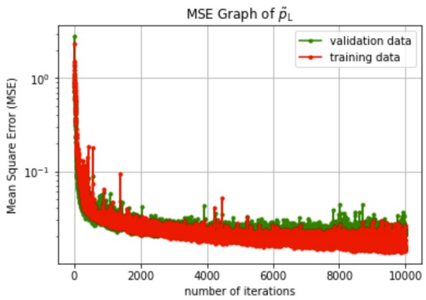

Figure 4.5: MSE Loss Graph with Applying Log Scale to $\widetilde{p}_L$ Predictions

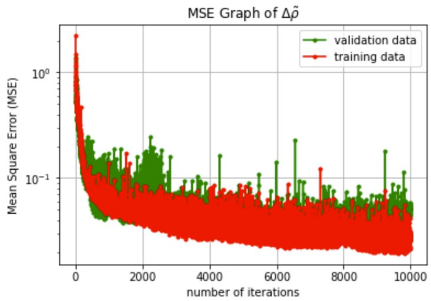

Figure 4.6: MSE Loss Graph with Applying Log Scale to $\Delta\widetilde{\rho}$ Predictions

In order to better show the convergence of the MSE loss of the model, log scaling is applied to MSE graphs. Log Scaling helped to observe the graphs more in detail. Figure 4.5 and 4.6 represents the log scaled version of the loss and the convergence of the error can be seen obviously. Although there are kind of variations in peaks in the graph, these could be negligible because this representation is in log scale. By means of it, log scale shows the error in a very low scale approximately 10^-2 which means that the curves can be considered as decreasing(converging) lines. Red Curve represents the training loss and the green curve that follows the red curve represents the test loss. Log scale also showed clearly that, test loss is almost as good as training loss with a little higher value. This again confirms that, there is no overfitting and a logical error graph is obtained.

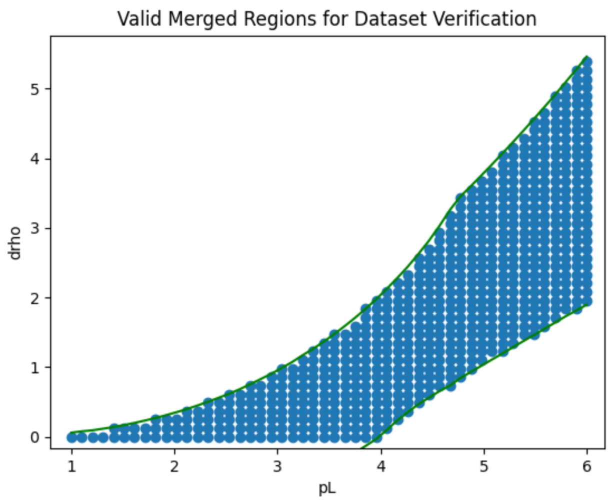

Figure 4.7: Merged Graph of Valid Regions

Figure 4.7 shows the artificially generated $\widetilde{p}_L$ and $\Delta\widetilde{\rho}$ values from valid regions. As it is explained in Section 3.2, synthetic pendant drop shapes are generated according to these artificially generated non-dimensional values. In Figure 4.7 is an illustration for the merged Valid Regions. Left and Right Valid regions are merged to show the whole Valid Region together.

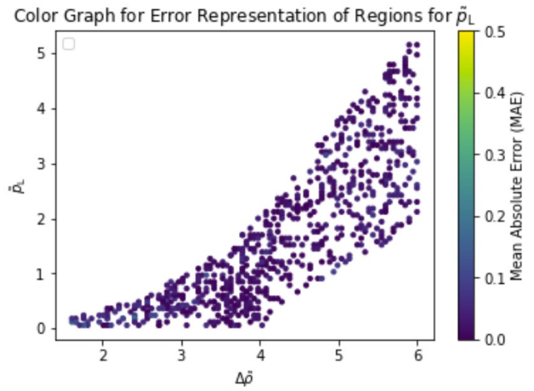

Figure 4.8: Colored Graph according to Prediction Performance of $\widetilde{p}_L$

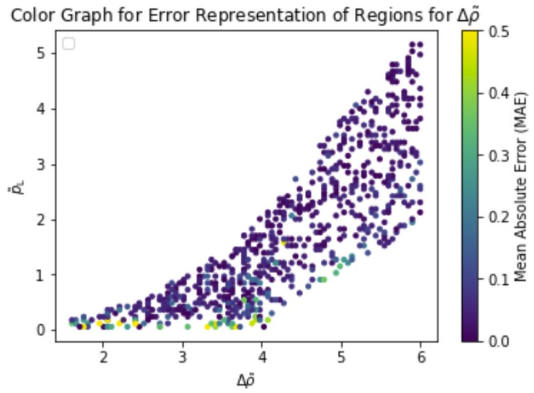

Figure 4.9: Colored Graph according to Prediction Performance of $\Delta\widetilde{\rho}$

Figures 4.8 and 4.9 represents the predictions that are made by Neural Network model. The objective is to obtain a representation that is very similar to Figure 4.7. Color bar in Figure 4.8 and 4.9 shows the success in the predictions. In Figure 4.8 if the Mean Absolute Relative Error (MARE) is above 0.16 the predicted $\widetilde{p}_L$ point is represented by yellow and if the MARE is less than 0.02 the predicted $\widetilde{p}_L$ point is represented by dark blue. These boundary values for prediction performance is 0.2 and 0.05 for Figure 4.9 which represents the predictio performance in $\Delta\widetilde{\rho}$ prediction. There is only one yellow point for both of the non-dimensional value predictions but almost every prediciton is dark blue. This shows the success of the Neural Network model.

Most erroneous predictions are close to the boundaries of the Valid Region. While drawing the curves of boundaries in Python and digitizing the graph using plot digitizer tool [28] there could be erroneous points for drawing the boundary curves of the Valid Region. This could be the reason of predicting the non-dimensional values worse in these parts of the region.

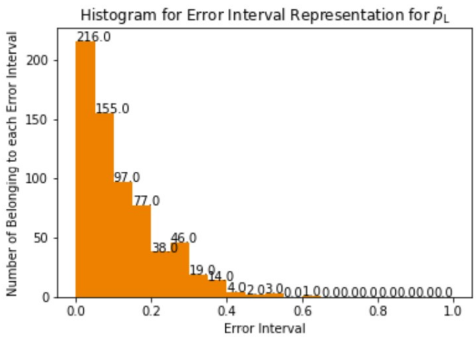

Figure 4.10: Histogram of Absolute Error for $\widetilde{p}_L$ Predictions

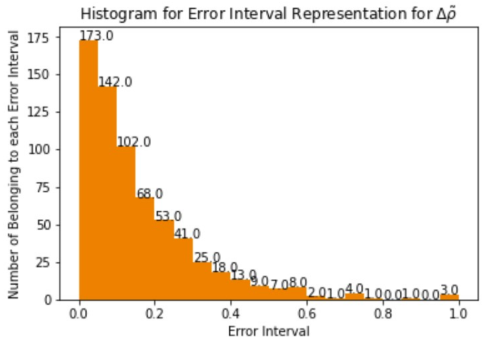

Figure 4.11: Histogram of Absolute Error for $\Delta\widetilde{\rho}$ Predictions

Figure 4.10 and 4.11 shows the histogram of predictions according to their *Absolute Error*. Histogram blocks are divided into intervals with 0.05. If the *Absolute Error* between prediction and true value less than 0.05, it will be placed to the first block and so on. Both Figures 4.10 and 4.11 are another proof of the success of the model since most of the predictions located in the first two blocks which means that the Absolute Error is less than 0.1.

Absolute Error is a kind of metric for visualizing the *digit matching* issue between predictions and true values. If the absolute error is less than 0.1, then almost the first 3 digits of prediction values are matching with the first 3 digits of true values. If the absolute error is less than 0.2, then almost the first 2 digits of prediction values are matching with the first 2 digits of true values. This is another kind of point of view to an error interpretation.

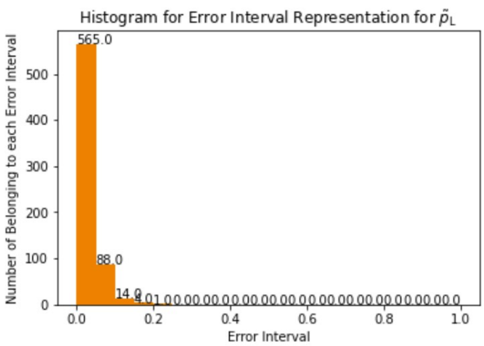

Figure 4.12: Histogram of Relative Error for $\widetilde{p}_L$ Predictions

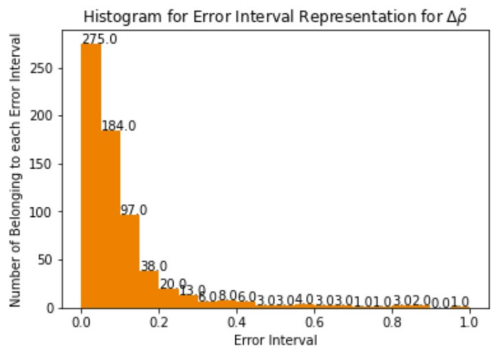

Figure 4.13: Histogram of Relative Error for $\Delta\widetilde{\rho}$ Predictions

Figure 4.12 and 4.13 shows the histogram of predictions according to their *Relative Error*. Histogram blocks are divided again into intervals with 0.05. Both

Figures 4.12 and 4.13 are another proof of the success of the model since most of the predictions located in the first two blocks which means that the Relative Error is less than 0.1.

When these histograms are compared with the previous histograms, it is expected that the number of errors belong to first two blocks should be higher. For example, there are 483 predictions in first three block of Figure 4.11 but there are 531 predicitons in first three blocks of Figure 4.13. This scenario is much vivid for 4.10 and 4.12. This difference for 4.12 and 4.13 between $\widetilde{p}_L$ and $\Delta\widetilde{\rho}$ predictions caused by the difference in the magnitudes of true values of $\widetilde{p}_L$ and $\Delta\widetilde{\rho}$ which are predicted. Range of $\widetilde{p}_L$ is [1,6] but range of $\Delta\widetilde{\rho}$ is [0,5]. Generated $\widetilde{p}_L$ values are bigger than generated $\Delta\widetilde{\rho}$ values. That's why the number of samples which has lower relative error is more in Figure 4.12.

MSE / L2 Loss / Quadratic Loss	$\dfrac{\sum_{i=1}^{N}\left(y_i - \hat{y}_i\right)^2}{N}$
Absolute Error	$\lvert\hat{y}_i - y_i\rvert$
Absolute Relative Error	$\dfrac{\lvert\hat{y}_i - y_i\rvert}{y_i}$
Regression Score Function	$R^2 = 1 - \dfrac{RSS}{TSS}$

Table 4.1: Table for Used Error Metrics for Performance Evaluation

Error metrics used for graph representations are illustrated in Table 4.1. MSE is the main metric which is also used for the loss calculation. For the other error metrics, mean is not calculated because giving the feeling of digit matching was vital at this point which is mentioned previously in this section. Absolute operator is applied because the predictions could be also lower than the true values which coould cause negative errors. Using absolute, this problem is eliminated.

Approximately 0.017 MSE loss is achieved for $\widetilde{p}_L$ prediction and apprximately 0.04 MSE loss is achieved for $\Delta\widetilde{\rho}$ prediction which are quite low values and as successful as previous works in terms of error. Additionally, R^2 value is calculated to measure the performance of predictions. Since non-dimensional values are regressed, using a regression score function is logical to evaluate the results. This metric has a range of [0,1] and if the R^2 value is close to 0, predictions are bad vice versa. This thesis work achieved to approximately 0.98 and 0.97 for $\widetilde{p}_L$ and $\Delta\widetilde{\rho}$ predictions respectively. R^2 values are almost 1 which shows that regressions are successful.

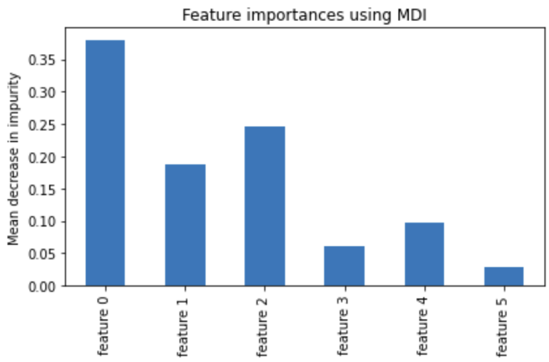

Figure 4.14: Feature Importances for Regression using 6 Features

Figure 4.14 shows the *Feature Importance* graph for the Neural Network Model and the first feature is the most important one which is the first Hu Moment and the second important one is feature 2(Third Hu Moment). Moments follows the increasing order and the feature 5 corresponds to the sixth Hu Moment.

After observing the feature importance, the relation between features are also investigated. While making a literature review, Flusser [33] made a research about the dependence/independence of Hu Moments which states that some of the moments are dependent. Then, covariance matrix of the features are printed to investigate the dependence of Hu Moments in the Neural Network model. Covariance Matrix is shown in Figure 4.15 in which the fourth, fifth and sixth moments are correlated. These correlation levels are depicted with colors in the colorbar. Correlation could be maximum 1 which is represented by yellow color. When the color is darker correlation between features are decreased and get closer to zero. Combining this information with feature importances, fourth and fifth Hu Moments are dropped because these moments has the lowest importance and has correlation. After removing these two moments new covariance matrix is plotted as in Figure 4.16 and model is trained for 4 Image Moments.

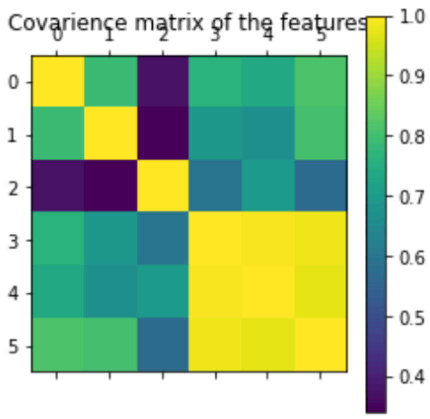

Figure 4.15: Covariance Matrix of Features(6 Hu Moments)

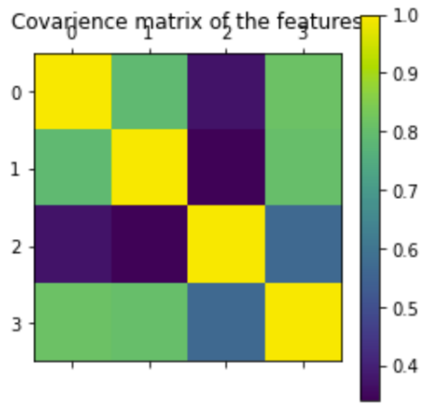

Figure 4.16: Covariance Matrix of Features(4 Hu Moments)

All the error metrics are computed again for the model with 4 Image Moments and no significant changes are observed and still model regresses the non-dimensional values successfully. Eventually, even simpler model is obtained than it is expected.

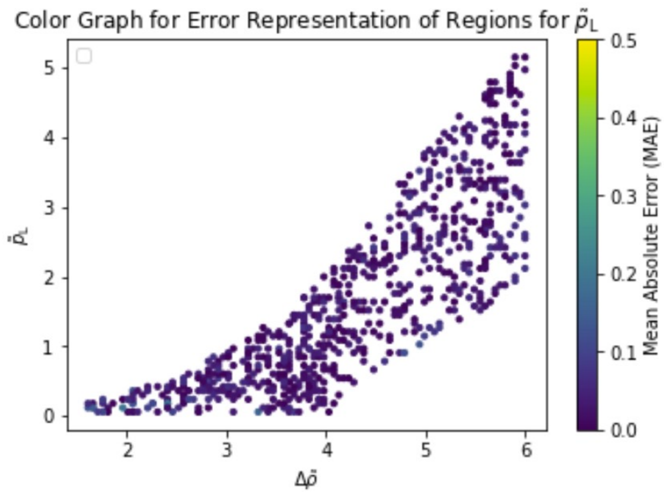

Figure 4.17: Colored Graph according to Prediction Performance of $\widetilde{p}_L$ with 4 Hu Moments

To better show the results, performances are depicted via again using the colored scatter plots for regressions of non-dimensional parameters. These graphs are shown in Figure 4.8 and 4.17. Performance is almost same for the model which has 4 features(4 models) and the training duration decreased too.

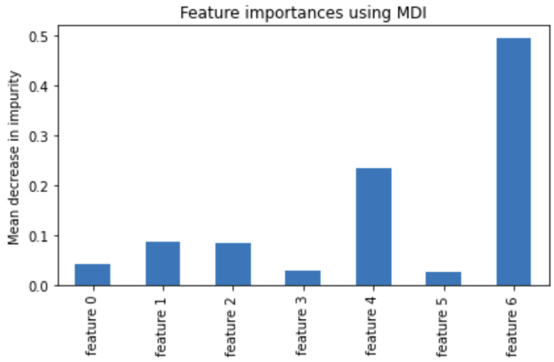

Figure 4.18: Feature Importance for Regression using 7 Features

Another testing is done by increasing the number of features by adding *Number of Events* parameter to the model. This parameter is explained in Section 2.4.2 and changes according to Valid Region. Adding this features does not help to improve the performance. On the contrary, regression performance decreased significantly because number of events feature dominated the model. Figure 4.18 shows the feature importance for regression and feature 6 stands for the number of events parameter. It highly dominates the model since it could be only two values which are '2' and '3'. MSE, absolute error are increased and regression score function becomes more close to 0 which are the proofs of the performance decrease.

Table 4.2: 5 Randomly Chosen Prediction of $\widetilde{p}_L$

$\widetilde{p}_L$ True	$\widetilde{p}_L$ Predictions
3.22	3.319
1.66	1.696
3.73	3.727
2.97	2.871
5.55	5.463

Table 4.3: 5 Randomly Chosen Prediction of $\Delta\widetilde{\rho}$

$\Delta\widetilde{\rho}$ True	$\Delta\widetilde{\rho}$ Predictions
0.848	0.908
0.121	0.185
0.818	0.808
0.606	0.610
3.39	3.291

Tables 4.2 and 4.3 shows 5 randomly chosen prediction results. These tables are to better understand what are the values of non-dimensional predictions and how they are regressed. Tables show one more time that, predictions are successful even if the regressed true values are so close to eachother. In other words, model is sensitive to small changes too. Each true value is the correspondent value for each other. For example, drop shape's $\widetilde{p}_L$ value is 3.22 and $\Delta\widetilde{\rho}$ value is 0.848. Their regression results are 3.319 and 0.908 respectively.

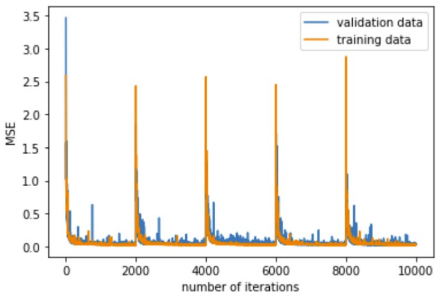

Figure 4.19: MSE Loss Graph with Applying K-Fold Cross Validation to $\widetilde{p}_L$ Predictions

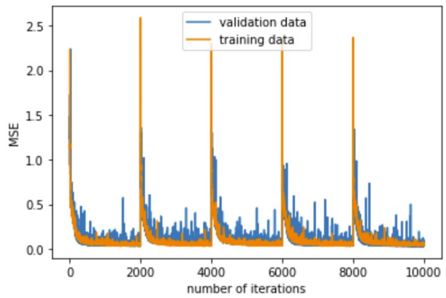

Figure 4.20: MSE Loss Graph with Applying K-Fold Cross Validation to $\Delta\widetilde{\rho}$ Predictions

Last but not least, *K-Fold Cross Validation* is also applied in order to prove that the obtained successful results are not obtained by chance. K-Fold Cross Validation is done when limited amount of data is available. Dataset is divided into K subsets. Training is done for $K - 1$ subsets and the last subset is used as test set. This process is done for K times when all the subsets are used as test sets. Avarage error is calculated over the K iterations to obtain a logical test error. Figure 4.19 and 4.20 are the MSE graphs for all cross validation phases. There are 5 peaks so 5-Fold Cross Validation is applied and MSE is calculated in 5 different iteration. Avarage MSE on test set through 5 iterations for $\widetilde{p}_L$ regression is 0.038 and avarage MSE for $\Delta\widetilde{\rho}$ regression is 0.045. These MSE losses are slightly high from our base model's erorrs but they are still very low and successful results. Consequently, the model is validated by using another metric again.

Chapter 5

Conclusion and Future Works

The proposed solution in this thesis work aimed to solve a problem for measuring Surface Tension of a pendant drop. While aiming measuring the Surface Tension of a pendant drop, a gap in this are is filled with bringing an innovative and simpler Machine Learning approach to this field. Since there are very rare works with Machine Learning approach in Pendant Drop Tensiometry method, this work has a special place in this area. A model is implemented for any user who aims to measure surface tension of a pendant drop so it can be widely used. Surface Tension of a pendant drop can be regressed by using Image Moments together with a Neural Network architecture was the hypothesis in the beginning. Chapter 4 verified the hypothesis and successfull results are obtained. The main aim during regressing the Surface Tension is to bring innovative and simpler model in which the 'innovation' is using Image Moments together with a Neural Networks model and 'simpler' part is a less complex and less computationally demanding solution. Both aims was achieved by this model and similar error rates compare to previous successful works were achieved in this thesis.

Different improvements also applied during the implementation process. First, thesis started with 7 Image Moments, it is decreased to 6, then covariance matrix analysis makes removing 2 more moments possible for a simler solution. During verifying the model's success different verification methods and error metrics are used such as K-Fold Cross Validation, Scatter Plots, Colored Graphs, Regression Score Function and MSE. After observing all the results, error rates brought successful results.

For future works, the first development could be increasing the number of samples in the dataset. To obtain a better result for this purpose, K-Fold Cross Validation is used. Another improvement could be switching to Real Images instead of Synthetic Images or a dataset could be generated by mixing both Real and Synthetic Images. In this way the results in this thesis could be further validated. There aren't much Real Image to use for this purpose in this project so all the images used in this project are Synthetic Images. When capturing Real pendant drop images some problematic issues could be occur in terms of camera and light source. Optical aberrations should be eliminated in that case to prepare a proper pendant drop image. While adding real images to training and test set image resolution limitation could also be tested by generating images which have different resolutions and whose size is more than $150x150$.

To conclude, one last improvement could be using a different Neural Network type such as CNN. CNN is widely used for image related problems and solves image related problems with high performance. CNN could be applied with or without Image Moments to regress the Surface Tension of e pendant drop from an image.

Bibliography

[1] Joseph D. Berry, Michael J. Neeson, Raymond R. Dagastine, Derek Y.C. Chan, and Rico F. Tabor. «Measurement of surface and interfacial tension using pendant drop tensiometry». In: *Journal of Colloid and Interface Science* 454 (2015), pp. 226–237. ISSN: 0021-9797. DOI: https://doi.org/10.1016/j.jcis.2015.05.012. URL: https://www.sciencedirect.com/science/article/pii/S002197971500466X (cit. on pp. i, 2, 6, 21–23, 25, 27, 31).

[2] Felix S. Kratz and Jan Kierfeld. «Pendant drop tensiometry: A machine learning approach». In: *The Journal of Chemical Physics* 153.9 (Sept. 2020), p. 094102. ISSN: 1089-7690. DOI: 10.1063/5.0018814. URL: http://dx.doi.org/10.1063/5.0018814 (cit. on pp. i, ii, 1, 8, 21, 23–32, 35, 40, 42).

[3] Susanna Laurén. *What is the difference between surface and interfacial tension?* https://www.biolinscientific.com/blog/what-is-the-difference-between-surface-and-interfacial-tension (cit. on p. 2).

[4] *Surface tension.* https://en.wikipedia.org/wiki/Surface_tension (cit. on pp. 2, 3).

[5] *Interfacial tension.* https://www.kruss-scientific.com/en/know-how/glossary/interfacial-tension (cit. on pp. 3, 7).

[6] Arthur Mason Worthington. «II. On pendent drops». In: *Proceedings of the Royal Society of London* 32.212-215 (1881), pp. 362–377 (cit. on p. 4).

[7] F. Bashforth and J.C. Adams. *An Attempt to Test the Theories of Capillary Action by Comparing the Theoretical and Measured Forms of Drops of Fluid.* Creative Media Partners, LLC, 2019. ISBN: 9781010107026. URL: https://books.google.de/books?id=2eW0wwEACAAJ (cit. on pp. 4, 21).

[8] *Pendant Drop.* https://www.kruss-scientific.com/en/know-how/glossary/pendant-drop (cit. on p. 4).

[9] DataPhysics Instruments GmbH. *Prodcuts.* https://www.dataphysics-instruments.com/products/ (cit. on p. 5).

[10] Jaroslaw Drelich, Ch Fang, and Calvin White. «"Measurement of Interfacial Tension in Fluid/Fluid Systems" J. Drelich, Ch. Fang, and C. L. White, pp. 3152-3166 in the Encyclopedia of Surface and Colloid Science, Marcel- Dekker, 2002.» In: Jan. 2002, pp. 3152–3166 (cit. on pp. 6, 7).

[11] Joseph D. Berry, Michael J. Neeson, Raymond R. Dagastine, Derek Y.C. Chan, and Rico F. Tabor. *OpenDrop*. `https://github.com/jdber1/opendrop/tree/master/example_images` (cit. on p. 8).

[12] Google. *Interest Over Time-Deep Learning*. `https://trends.google.com/trends/?geo=GB` (cit. on p. 13).

[13] Jan Flusser, Barbara Zitova, and Tomas Suk. *Moments and Moment Invariants in Pattern Recognition*. Wiley Publishing, 2009. ISBN: 0470699876 (cit. on pp. 16–18, 20).

[14] Ming-Kuei Hu. «Visual pattern recognition by moment invariants». In: *IRE Transactions on Information Theory* 8.2 (1962), pp. 179–187. DOI: `10.1109/TIT.1962.1057692` (cit. on pp. 16, 18, 20).

[15] Yaser Daanial Khan, Farooq Ahmed, and Sher Afzal Khan. «Situation recognition using image moments and recurrent neural networks». In: *Neural Computing and Applications* 24 (2013), pp. 1519–1529 (cit. on pp. 16, 20).

[16] *Shape Matching using Hu Moments (C++/Python)*. `https://learnopencv.com/shape-matching-using-hu-moments-c-python/` (cit. on pp. 19, 30, 39).

[17] J. Flusser, T. Suk, and S. Saic. «Recognition of blurred images by the method of moments». In: *IEEE Transactions on Image Processing* 5.3 (1996), pp. 533–538. DOI: `10.1109/83.491327` (cit. on p. 19).

[18] George Papakostas. «Over 50 Years of Image Moments and Moment Invariants». In: July 2014, pp. 3–32. ISBN: 9786188141803. DOI: `10.15579/gcsr.vol1.ch1` (cit. on p. 20).

[19] Andre Barczak, Martin Johnson, and Chris Messom. «Revisiting moment invariants: rapid feature extraction and classification for handwritten digits». In: (Jan. 2007) (cit. on p. 20).

[20] Matheesha Fernando and Janaka Wijayanayake. «Novel Approach to Use HU Moments with Image Processing Techniques for Real Time Sign Language Communication». In: *International Journal of Image Processing (IJIP)* 9 (Dec. 2015) (cit. on p. 20).

[21] Y. M. Zhao, Wenfang Xie, and T. T. Wang. «Neural network-based image moments for visual servoing of planar objects». In: *2012 IEEE/ASME International Conference on Advanced Intelligent Mechatronics (AIM)* (2012), pp. 268–273 (cit. on p. 20).

[22] Sanad Aburass, Ammar Huneiti, and Mohammad Belal. «Enhancing Convolutional Neural Network using Hu's Moments». In: *International Journal of Advanced Computer Science and Applications* 11 (Jan. 2020). DOI: 10.14569/IJACSA.2020.0111216 (cit. on p. 20).

[23] A C Merrington and E G Richardson. «The break-up of liquid jets». In: *Proceedings of the Physical Society* 59.1 (Jan. 1947), pp. 1–13. DOI: 10.1088/0959-5309/59/1/302. URL: https://doi.org/10.1088/0959-5309/59/1/302 (cit. on p. 21).

[24] W.N. Bond M.A. D.Sc. F.Inst.P. and Dorothy A. Newton B.Sc. «LXXXII. Bubbles, drops, and Stokes' law. (Paper 2)». In: *The London, Edinburgh, and Dublin Philosophical Magazine and Journal of Science* 5.30 (1928), pp. 794–800. DOI: 10.1080/14786440408564523. eprint: https://doi.org/10.1080/14786440408564523. URL: https://doi.org/10.1080/14786440408564523 (cit. on p. 21).

[25] M. A. Cabrerizo-Vilchez, J. R. Fernández, M. A. Fernández-Rodríguez, L. García-Río, M. C. Muñiz, and Cristina Núñez. «Interfacial tension measurements using a new axisymmetric drop/bubble shape technique». In: *RSC Adv.* 9 (28 2019), pp. 16187–16194. DOI: 10.1039/C9RA00940J. URL: http://dx.doi.org/10.1039/C9RA00940J (cit. on p. 28).

[26] Lorenzo Busoni, Marcello Carla, and Leonardo Lanzi. «Algorithms for fast axisymmetric drop shape analysis measurements by a charge coupled device video camera and simulation procedure for test and evaluation». In: *Review of Scientific Instruments* 72 (June 2001), pp. 2784–2791. DOI: 10.1063/1.1364666 (cit. on p. 28).

[27] Conrado Ferrera, Jose Montanero, and M. Cabezas. «An analysis of the sensitivity of pendant drops and liquid bridges to measure the interfacial tension». In: *Measurement Science and Technology* 18 (Oct. 2007), p. 3713. DOI: 10.1088/0957-0233/18/12/006 (cit. on p. 28).

[28] *web Plot Digitizer*. https://apps.automeris.io/wpd/ (cit. on pp. 32, 44).

[29] *scipy.integrate.solve ivp*. https://docs.scipy.org/doc/scipy/reference/generated/scipy.integrate.solve_ivp.html (cit. on p. 35).

[30] J.R. Dormand and P.J. Prince. «A family of embedded Runge-Kutta formulae». In: *Journal of Computational and Applied Mathematics* 6.1 (1980), pp. 19–26. ISSN: 0377-0427. DOI: https://doi.org/10.1016/0771-050X(80)90013-3. URL: https://www.sciencedirect.com/science/article/pii/0771050X80900133 (cit. on p. 35).

[31] Zhihu Huang and Jinsong Leng. «Analysis of Hu's moment invariants on image scaling and rotation». In: *2010 2nd International Conference on Computer Engineering and Technology*. Vol. 7. 2010, pp. V7-476-V7–480. DOI: 10.1109/ICCET.2010.5485542 (cit. on p. 37).

[32] Maxim M. Mizotin. «Subpixel Edge Detection in the Problem of Determining the Surface Tension from an Axisymmetric Drop Profile». In: *Computational Mathematics and Modeling* 25 (2014), pp. 365–380 (cit. on p. 37).

[33] Jan Flusser. «On the independence of rotation moment invariants». In: *Pattern Recognition* 33 (2000), pp. 1405–1410 (cit. on p. 47).